



UNIVERSITATEA
LUCIAN BLAGA
— DIN SIBIU —



Interdisciplinary Doctoral School

Doctoral field: Industrial Engineering

**Developing a Procedure and Device Based on
Dynamic Light Scattering for Assessing the Particle
Size in Technological Fluids**

- Abstract -

PhD Candidates:

Sorin Olaru

Scientific coordinator:

Proffesor, PhD. ENG. Dan Chicea

Table of Contents

Keywords	3
1. Particles, types, and their classification	4
2. Traditional physical methods of particle characterization.	6
3. Optical methods for characterisation of particles	10
4. DLS equipment.....	17
5. Optical sensors.....	20
6. Optical detector. Functional blocks, practical design, and realization	24
7. – Amplification and linearity measurements	29
8. Particulate measurements using the stepwise filter filtration method	34
9. Measurement of particulate size in air (smoke and aerosols) using DLS technique	38
10. Measurement of particle size in air using DLS technique on an aqueous suspension containing wind-borne Sahara dust particles	48
11. Particle size measurement of automotive fluids (brake fluid and coolant) using DLS technology	57
Conclusions	62
Annex - List of publications, participation in conferences and research projects.....	64
Bibliography	65

Keywords

Dynamic light scattering, DLS, time series, particle characterization, micro-particles, nanoparticles, technological fluids, measurements, signal acquisition, signal processing.

1. Particles, types, and their classification

According to the general understanding, a particle is a small fragment or discrete relatively small or smallest quantity of something. Because the word "small" is relative to "something," a particle can be as small as a quark or as large as the sun. Relative to the vastness of the universe, the sun is nothing but a tiny particle. That's why the range of technologies and sciences that deal with the study of particles extends from high-energy physics to astrophysics. To begin with, we will need to define the types of particles that are the subject of this study and that interest us. Their sizes range from a few nanometers to micrometer sizes. We will call them industrial particles.

They can exist in some very different forms. They can be natural or synthetic macromolecules, in linear form or in networks (proteins, gels, latexes, etc.). The particles can be conglomerates of inorganic or organic molecules (micelles, liposomes) or even voids such as bubbles in solid or liquid foams. The presence of particulate matter materials is ubiquitous: from materials and substances used in household appliances, to ingredients in food and beverages, and from transport vehicles of all kinds and installations in industry, to substances used in the pharmaceutical industry. Particles have a profound impact on life, and we can say that everyone has dealt with particles, in one way or another, at some point in their daily lives.

Industrial particles cover a wide range of sizes. For example, contaminants can cover five orders of magnitude, and dust covers about seven orders of magnitude, from decimeters to submicrons. Figure 1 shows some typical industrial particles and their approximate size ranges:

10^{-2}m		rain				
10^{-3}m	sand					
10^{-4}m						
10^{-5}m	mud	mist				
10^{-6}m			ash		bacteria	
10^{-7}m	clay	smog		paint pigments		oil vapour
10^{-8}m			smoke		viruses	
10^{-9}m						

Fig. 1: Approximate size ranges for industrial particles

In this size regime, a particle can be either a high molecular weight molecule or a group of molecules. The latter can be molecular associations or just different forms of particles. From the point of view of physical chemistry, industrial particle systems, regardless of their chemical compositions and practical applications, are dispersions, except for solutions of macromolecules.

Generally, for a particle sample, there are two types of properties. One is the properties of the material, such as its elemental composition, molecular structure, or crystal structure, which are independent of the macroscopic form of presence. Whether in bulk form (solid or liquid) or in particle form, these properties will not vary. The other class of properties, such as geometric properties of individual particles (size, shape, and surface structure), is closely associated with the fact that the material is in the form of particles. For particle material, in addition to the properties of individual particles, many bulk characteristics, such as explosiveness, carrying capacity, gas

permeability and powder compressibility, are also related to the fact that the material is in particle form. These properties will not be present if the material is in overall form. If we dedicate the phrase "particle characterization" to measurements related to the properties of the second type, then the phrase "particle analysis" can be, as often happens, for measurements related to the properties of the first type. The technologies used in particle analysis are quite different from those used for particle characterization.

Most physical properties of a particle system are assemblies or statistical values of properties from their individual constituents. The geometric properties of commonly evaluated particles are counts, size (size and distribution), shape (or conformation), and surface characteristics (specific area, charge and distribution, porosity and distribution). Among these properties, characterization of particle size and surface characteristics is of key interest. The behavior of a particle system and many of its physical parameters are highly dependent on size. For example, viscosity, flow characteristics, filtrability of suspensions, reaction rate and chemical activity of a particle system, stability of emulsions and suspensions, abrasiveness of dry powders, color and finish of colloidal paints and paper coatings, strength of ceramics, are all dependent on particle size distribution. Out of necessity, there are many technologies that have been successfully developed and used in particle characterization, especially those for sizing particles from nanometers to millimeters. Before the adoption of modern and light-based technologies, most particle sizing methods were based either on physical separation of a sample, such as sieve analysis, or on analysis of a limited number of particles, as in the microscopic method. In recent decades, thanks to the advent and commercialization of lasers and microelectronics (including high-performance computers), the science and technology of particle characterization has advanced a lot. Today, many new and sophisticated technologies have been successfully developed and applied in particle characterization. Some previously popular characterization methods are now being removed from many areas.

The choice of an appropriate method for particulate characterisation depends entirely on the requirements of the application and the availability of an appropriate technique. A compromise is often made when choosing the best method for characterizing materials in particle form.

2. Traditional physical methods of particle characterization.

Following are some more common methods of particle characterization other than methods using the analysis of light scattering dynamics currently used in various industrial applications. The principles for each method are presented along with the general range of application, advantages, and disadvantages.

SIEVE analysis (5 μ m-10cm) – sieve analysis uses a test sieve, which has a screen with many uniform openings to classify materials into different fractions. The fraction of material that is larger than the screen opening will be retained on the screen, and the fraction that is smaller than the aperture will pass. Openings are either gaps between threads woven into a wire sieve in which the screen is a piece of metal or nylon cloth, or holes drilled in a metal plate in a sieve with perforated sheet metal, or photo-etched holes in a sheet of metal in an electroformed sieve. Due to the simplicity of the principle, equipment and analytical procedure, sieve analysis has been widely used in almost all areas requiring the sizing of particles larger than several tens of microns.

Despite its wide use, there are several drawbacks inherent in this method. The openings on a sieve are actually three-dimensional, given the round woven threads. Whether a three-dimensional particle of any shape will be able to pass through an opening depends on the orientation of the particle. Usually, the result of sieve analysis varies depending on the method of moving the sieve or particles, the geometry of the sieve surface, the service life, the number of particles on the sieve and the physical properties of the particles.

Sedimentation method (0.05 μ m -100 μ m) - *sedimentation* is also a classical method of classifying and sizing particles for liquid particles. Sedimentation methods are based on the rate of sedimentation of particles in a liquid at rest under a gravitational or centrifugal field. The relationship between settling rate and particle size is reduced to the Stokes equation at reduced Reynolds numbers:

$$d_{St} = \sqrt{\frac{18\eta u}{(\rho_s - \rho_l)g}} \quad (1)$$

In equation (19), d_{St} is the diameter of Stokes that is equal to the equivalent diameter of a spherical particle that has the same density and free fall velocity as the real particle in the same liquid under laminar flow conditions. The quantities η , u and g are the viscosity of the suspended liquid, the stabilization rate of the particles, the effective density of the particles, the density of the liquid and the acceleration. In gravitational sedimentation methods, g is the gravitational acceleration and in centrifugal sedimentation methods, g ($= \omega^2 r$ with ω and r being the angular velocity of the centrifugation and the radius where particles are measured, respectively) is centrifugal acceleration.

The basis of a sedimentation experiment to infer information about particle size is the Stokes equation, which holds for a single spherical particle that slowly settles into a fluid of infinite extent without interference from other forces or motions. To satisfy these conditions, the experiment should be carried out only at low concentrations and for particles within a certain size range. At high concentrations there are mutual interactions or interferences between particles.

Laminar flow cannot be maintained either for very large particles, whose velocities are so high that vortices or turbulence will form, or for very small particles, where the disturbance of free settling due to the Brownian motion of the particles is too great.

Sedimentation methods have been widely used in the past and many product specifications and industry standards have been established based on these methods. However, there are intrinsic limitations associated with sedimentation. For a non-spherical particle, its orientation is random at a reduced Reynolds number, so it will have a wide range of settling velocities. As the Reynolds number increases, the particle will tend to orient itself to create maximum resistance and settle at its lowest velocity. Thus, for a polydisperse sample of non-spherical particles, there will be a trend in the size distribution towards larger particles and the result obtained will be wider than the actual distribution. In addition, all samples analysed using sedimentation must have a uniform and known density, otherwise particles of different sizes may settle at the same rate due to density variations.

Electrical detection method (Coulter principle) (0.4 μm -1200 μm) - a tube with a hole or opening is placed in an electrolyte solution containing particles of interest in low concentration. The device has two electrodes, one inside and the other outside the hole. The aperture creates what is called a detection zone. The particles pass through the diaphragm when liquid is extracted from one side. As a particle passes through the detection area, a volume of electrolyte equivalent to the submerged volume of the particle is displaced from the detection area. This causes a short-term change in resistance along the diaphragm. This change in resistance can be measured as a voltage pulse or as a current pulse. By measuring the number of pulses and their amplitudes, information can be obtained about the number of particles and the volume of each individual particle. The number of pulses detected during measurement is the number of particles measured, and the pulse amplitude is proportional to the volume of the particle:

$$U = \frac{V\rho_0if}{\pi^2R^4} \quad (2)$$

In equation (2), U, V, ρ_0 , i, f and R are the voltage pulse amplitude, particle volume, electrolyte resistivity, current through the diaphragm, particle "form" factor, and diaphragm radius. If a constant particle density is assumed, the momentum height is proportional to the mass of the particles. The measured particle size can be channeled using the pulse height analyzer circuit and a particle size distribution is thus obtained. The instrument's electrical response is essentially shape-independent for particles of the same volume, both in theory and practice.

The lower dimension limit of this method is defined by the ability to discriminate all types of noise from the signal generated by particles passing through the opening. The advantages of the method are that it measures the volume of a particle and the result will only be influenced by the shape of the particle in extreme cases, and that it can count and measure simultaneously with very high resolution and reproducibility. However, the limitation or disadvantage of this method lies in the fact that the particles that can be analyzed are limited to those that can be dispersed in an electrolyte solution and still retain their original integrity.

Image Analysis - Microscopic Methods - Morphology and Sizing Study (0.001-200 μm) and Holographic Method - Sizing (0.3-1000 μm) - Microscopic methods include an image capture

procedure, image processing and analysis procedure. In capturing images process you must pay attention to sample preparation so that representative particles from the sample are taken and seen. There should be a minimum number of particles touching and any staining, shading, or coating of the particles should not lead to incorrect information.

Conventionally, images captured from microscopic measurements are recorded on photographic papers, followed by manual study of the shape, size, or morphology of the particle surface in the images. These images can then be reprocessed and analyzed using an image analysis program. Particle size measurement (cable size, area, and length), particle number, and shape analysis can be achieved by image analysis.

Microscopic analysis has advantages over other methods in that it can provide information about size, shape, surface texture and some optical properties of individual particles in a wide range of sizes and in detail. However, the major disadvantage of microscopic methods is that in most cases, they only produce information from 2D projected areas of particles. The orientation of the particles in the prepared sample can significantly alter the result. Another big disadvantage is that, despite modern automatic image analysis, the number of focused particles that can be inspected in whichever viewing range you choose is limited. Thus, for a polydisperse sample, an adequate statistical representation of the entire sample can be a complex, if not nearly impossible, task.

The holographic method assumes that images are formed in a two-step process. In the first step, a collimated coherent light is used to illuminate the sample. A hologram consists of the far-field diffraction patterns of all particles in the illuminated sample volume, with coherent illuminating light as the background. Many individual diffraction patterns overlap in the 2D hologram.

In the second step, the hologram is again illuminated by a coherent light source and a stationary image of all particles is created at their original locations in the volume. This three-dimensional image can be studied and restudied by focusing the visual plane on the particles at different locations, and new 2D images of the particles can then be visualized or recorded. The same image analysis tools used in microscopic studies can be used to analyze these holographic images to determine particle characteristics.

Since a hologram is recorded using a pulsed laser of very short duration, and because particles are recorded in their real medium (suspension, aerosols, etc.), this method records the sample at a given time. A more detailed study can be done in the second step at some point later. This method can provide information about particle size, shape, and even the orientation of particles in real space. Using a modified recording process and special mathematics, this technique can even measure the motion (velocity) of particles.

Sizing and measurement of submicron aerosols (0.001-1 μm) - submicron aerosol particles exist abundantly in the atmosphere but, due to their size and concentrations, common methods of sizing and counting are not suitable for direct measurement. The common procedure for

characterization of submicron particles has two steps. At the first stage, aerosol particles are fractionated according to their size. They then pass through a container of evaporative liquid. The vapor condenses on the aerosol, resulting in particles of much larger size, which can then be detected and counted by an optical meter. Two schemes can be used for fractionation of submicron aerosols. In the first scheme, called the battery diffusion method, particles pass through a stack of mesh screens. Due to diffusion, they will collide and be captured by the threads of the screen. Small particles will be captured first, as they diffuse rapidly and many more collisions will occur with the screen wires. Large particles will be captured by the resulting screens. Aerosol particles between 5 nm and 200 nm can be fractionated using the battery diffusion method. In the second scheme, called differential mobility analysis, particles are first charged and then carried by a carrier stream passing through an electric field. The particles are fractionated according to their differential electric mobilities and therefore different speeds, both of which are related to their dimensions. Particles between 1-1000nm in diameter can be fractionated in this way.

3. Optical methods for characterisation of particles

Light is electromagnetic radiation in the frequency range from about 10^{13} Hz (infrared) to 10^{17} Hz (ultraviolet), or with a wavelength between 3 nm and 30.000 nm. The conversion between frequency and wavelength of light can be done using the speed of light ($c = 3 \cdot 10^8$ m/s in vacuum):

$$c = \lambda\nu \quad (3)$$

Visible light is the part of electromagnetic radiation to which the human eye is sensitive. When white light, which contains a range of wavelengths, is separated into wavelengths, each wavelength is perceived as a different color. The wavelength of visible light ranges from ~400 nm (violet) to ~700 nm (red). As light propagates, it has the characteristics of both a transverse wave (a light wave) and a particle (a photon). As a wave, light has wave-like properties such as frequency, wavelength, and interference; As a particle, light has particle-like properties such as momentum, velocity, and position.

When a beam of light illuminates a piece of matter having a dielectric constant different from the unit, the light will be absorbed or scattered, or both, depending on the wavelength of light and the optical properties of the material. The net result of absorption and scattering caused by the material is known as the disappearance of incident light,

$$\textit{Extinction} = \textit{Absorption} + \textit{Scattering} \quad (4)$$

When light interacts with electrons bound in the material so that it radiates light, scattering is observed. The scattering detected is from particles in a scattering volume, in the cross-section between the beam and the detection cone. The energy of absorbed light, which becomes the excitation energy of particles, will be dissipated mainly by thermal degradation (i.e. converted into heat) or lost by radiative degradation, producing fluorescence or phosphorescence, depending on the electronic structure of the material. Since many materials exhibit strong absorption in infrared and ultraviolet regions, which greatly reduces the intensity of scattering, most light scattering measurements are performed using visible light. Scattering is observed only when a material is itself heterogeneous, either due to fluctuations in local density in the pure material or due to optical heterogeneity for particles dispersed in a medium. In a perfectly homogeneous and isotropic material, radiation scattered by individual molecules interferes destructively, and therefore no scattering is observed.

The intensity of scattering from a unit volume of material that is illuminated by a unit stream of light is a function of the complex ratio of the refractive index between the material and its environment, along with various other properties of the material. In the Rayleigh scattering regime, where the particle size is much smaller than the wavelength of light, the scattering intensity is inversely proportional to the fourth wavelength strength when the same material is illuminated by light of different wavelengths but having the same intensity, i.e., the shorter the wavelength, the stronger the scattering:

$$I_s \propto I_o/\lambda^4 \quad (5)$$

The photon correlation experiment was initiated in the 50s, but the popularity of this technology was possible only after coherent light sources from lasers became available at low cost in the 70s. Solving the distribution of Brownian motion in a solution of macromolecules or in a suspension of particles by photon correlation spectroscopy was practical only when electronic computing became fast enough that a user did not have to wait hours for the result.

In light scattering experiments, the collimated light source (polarized or non-polarized) must be at a much greater distance than the particle size to be measured and is used to illuminate the sample. The intensity of scattering is detected at a distant field (the distance, r , between the detector and the particle sample must be much larger than the particle size). In this way, the incident light and scattered light will behave like a plane wave, making the theoretical description simple. The cross-section between the incident light and the viewing cone of the detector defines the volume of scattering. In the scattering volume there can be only one particle, in the case of optical particle counting, or many particles. Scattering results from changes in the electric field of all particles in the scattering volume, illuminated by incident light. Since particles scatter light in all directions, the intensity received by the detector is proportional to the detection area and inversely proportional to the square of its distance from the dispersers. Although the liquid in which the suspension is located also scatters light, scattering can be neglected compared to the magnitude of dispersion from the particles. Exceptions to this we have when an inhomogeneous medium is used or when the mass of the particle is comparable to that of liquid molecules.

We assume that the incident light is a collimated beam having a flat wavefront and uniform intensity. In fact, an important purpose in designing the optics of a light-scattering instrument is to achieve a homogeneous beam intensity and reduce its divergence to a minimum.

Many light sources, such as a He-Ne laser, have a Gaussian intensity profile. The diameter of the beam is characterized by the circular region having a radius twice the standard deviation (2σ). Most of the light output is in this region, and the light intensity at 2σ radius from the center of the beam drops to 0.135 of the maximum intensity. For Gaussian or divergent beams, all given formulas must be modified accordingly, leading to generalized theories that have more complicated formulas.

The analytical formulation of scattering intensity from spheres of arbitrary size is currently widely used in many light-scattering technologies, in which the assumption of spherical particles is taken for granted. The following are the rigorous solution for scattering from spheres, followed by three theories that are approximations of scattering from particles either much smaller or much larger than the wavelength of light, and a summary of numerical computational approaches for scattering particles of other shapes.

Rigorous solution: Mie theory - Mie theory is a rigorous solution for the given scattering of spherical, homogeneous, isotropic, and non-magnetic particles of any diameter d in a non-absorbent medium. Although the theory is generally called the Mie theory or the Lorenz–Mie theory, it was actually developed based on several independent theoretical works by many theorists, including Lorenz and Mie.

For spheres, the angular scattering pattern is symmetrical with respect to the incident light axis, i.e. the scattering pattern is the same for the same absolute scattering angle value. In these models there are minimums and maximums of scattering at different locations, depending on the properties of the particles.

At small angles, usually less than 10 degrees, the scattering pattern for spheres is centrally symmetrical in addition to being axially symmetrical; that is, it displays concentric rings in the direction of propagation of the incident light. Within this range, the intensity will be the same for the same solid angle with respect to the incident light and is not limited to the angle θ in the plane of scattering relative to mass.

Zeroth order approximation: Rayleigh scattering - if a particle is much smaller than the wavelength of light, then each part of the particle will be exposed to the same homogeneous electric field (uniform instantaneous phase) of incident light and scattered light from the particle, and which will be the same as if scattered from an oscillating dipole radiating in all directions. This radiation is produced when an unpolarized particle (or molecule) is subjected to an electromagnetic wave. Its electric charges forcibly separate and an induced dipole moment is created, resulting in a polarized particle. This dipole is induced by the penetration of incident light into the particle due to the polarizability (α) of the particle in a short time compared to the light period. The dipole moment oscillates synchronously with the dipole field and moment axis and aligns with the electric vector of the incident wave. This type of scattering is called Rayleigh scattering. To satisfy the above approximation, the following two conditions must be met: 1) \ll size k_o^{-1} ; and 2) $|m| \cdot$ Size $\ll k_o^{-1}$. Here, size is the longest particle size. In general, α is a tensor; that is, it has three components along three perpendicular directions. For most optically isotropic materials, all three components are the same. The intensity of scattering is then related only to α , which is a function of the shape and volume of the particle. If the particle is isotropic, optically inactive, and the incident light is linearly polarized, all scattered light is linearly polarized. Equal amounts of light are scattered in the front and rear hemispheres. The spatial scattering intensity model has rotational symmetry around the dipole axis and a dependence on $\cos^2\phi$. At $\phi = 90^\circ$, the scattering is almost zero since there is no scattering in the direction of oscillation of the dipole moment. A 3-D scattering intensity model of a dipole on a polarized incident light has a tire-like shape with an infinitely small hole in the center that is the dipole.

The amplitude functions have the following values:

$$\begin{pmatrix} S_1 & S_4 \\ S_3 & S_2 \end{pmatrix} = ik_o^3 \alpha \begin{pmatrix} 1 & 0 \\ 0 & \cos\theta \end{pmatrix} \quad (6)$$

Thus, for natural light, we have the following Rayleigh equation:

$$I = \frac{(1 + \cos^2\theta)k_o^4 |\alpha|^2 I_o}{2r^2} \quad (7)$$

Since the length of the probe (wavelength of light) is much longer than the particle, no details can be found, except for the mass of the particle. The intensity of scattering varies as the second strength of the particle mass. Although α depends on the shape, all particles scatter light according to equation (7).

First order approximation: Rayleigh-Debye-Gans scattering - when the particle size is larger than that which can be treated as a single dipole, the approach is to treat the particle as an assembly of small and structureless scattering elements. Each of these scattering elements gives rise to Rayleigh scattering independently of other scattering elements in the particle. The phase shift corresponding to any element in the particle is negligible, and the phase difference between the different elements in the particle is determined only by their positions and is independent of the material properties of the particle. Scattering in each direction by all these elements results in interference due to the different locations of these elements in the particle. To satisfy the above assumptions, the particle must have a refractive index close to the medium ($|m-1| \ll 1$), in addition to being small compared to the wavelength of light ($|m-1| \cdot \text{size} \ll k_0^{-1}$). In Rayleigh-Debye-Gans theory, amplitude functions are summations of the scattering of all elements with a phase factor (δ) added to each element:

$$\begin{pmatrix} S_1 & S_4 \\ S_3 & S_2 \end{pmatrix} = \frac{ik_0^3(m-1)}{2\pi} \int e^{i\delta} dV \begin{pmatrix} 1 & 0 \\ 0 & \cos\theta \end{pmatrix} = \frac{ik_0^3(m-1)V}{2\pi} \sqrt{P(x)} \begin{pmatrix} 1 & 0 \\ 0 & \cos\theta \end{pmatrix} \quad (8a)$$

$$P(x) = (8b)V^{-2} \left| \int e^{i\delta} dV \right|^2 = n^{-2} \sum_i^* \sum_j \frac{\sin Kr_{ij}}{Kr_{ij}}$$

In equation (8), we took the polarizability α for a homogeneous particle when m is close to the unit to be $\alpha = (m^2-1) V/4\pi$. $P(x)$ is the scattering factor determined by the shape of the particle when m is real; that is, there is no absorption. $P(x)$ is derived from the consideration that a large particle has n identical active scattering centers, any two of which are separated by a spatial vector r_{ij} of length r_{ij} . All possible paired combinations of these centers in the geometry of particles form the basis of the scattering interference pattern. For many regular forms, scattering factors were derived. For most particles of regular shapes, scattering factors are a function of the product of their characteristic size and scattering vector. The x symbol is commonly used for this product. $P(x)$ can generally be formulated using a series expansion:

$$P(x) = 1 - \frac{K^2 R_g^2}{3} + \dots \quad (9)$$

where R_g is the radius of rotation of a particle, which is the effective radius of a body in terms of rotation, or the radius at which all mass is concentrated, defined by:

$$R_g^2 = \frac{\int \rho(r)r^2 dV}{\int \rho(r)dV} \quad (10)$$

where $p(r)$ is the mass density at r . When x is less than 0.25, the third and largest term in equation (9) can be abandoned. The initial slope of $P(x)$ with respect to K^2 is then related to the radius of rotation of the particles.

Scattering factors for optically anisotropic particles will have different shapes depending on the polarization of both incident and scattered light. The biggest advantage in using scattering factors is that these functions are independent of the refractive index of the particle. Once the experimental setup is determined, size and shape are the only variables. Thus, for small particles, once the shape of the particles is known, characterization of the size is easy provided that all

particles have the same geometric shape. For visible light, the Rayleigh-Debye-Gans theory can be used for particles up to several hundred nanometers in size.

Large end approximation: Fraunhofer Diffraction (The large-end approximation) - if the size of the particle is much larger than the wavelength of light, the target particle will emit an amount of light energy directly proportional to twice the area of its cross-section. An areal cross-section is eliminated by the sum of reflection, refraction and absorption, and a cross-sectional area by diffraction. For large particles, another rather different approach is used. When the particle size is much larger than the wavelength of light or the material is highly absorbent, the edge effect of the particles contributes much more to the total scattered intensity.

The interference effect now arises mainly from the contour of the particles; that is, diffraction produced by bending light at the edge of particles. In these cases, scattering from the inner part of the particle is less important and neglected as an approximation. For large particles, when only edge effects are considered, we can use various diffraction equations to describe scattering patterns. The particle now behaves like a two-dimensional object instead of a three-dimensional particle. Only the area projected perpendicular to the light matters, not the volume of the particles. Diffraction can be described by Huygen's principle: each point on a propagating wavefront is a secondary wave emitter. The locus of expansion waves forms the propagation wave. The interference between secondary waves gives rise to a fringe pattern, which rapidly decreases in intensity as the angle in the original direction of light propagation increases. Diffraction is an important physical effect inherent in all wave phenomena. There are two classes of diffraction, namely Fraunhofer diffraction and Fresnel.

Fraunhofer diffraction involves coherent plane waves that occur at an obstruction. Fresnel diffraction involves spherical waves incident to an obstruction. Experimentally, Fresnel diffraction is produced from a point source and Fraunhofer diffraction from a parallel beam. The Fraunhofer diffraction through an aperture is mathematically equivalent to the Fourier transform of the aperture shape. Because integrals describing Fresnel diffraction are difficult to treat, Fresnel diffraction models have few analytical solutions, even in one dimension.

The theories described above are based on time-mediated scattering intensity, with the assumptions that the dispersors do not move and that the intensity of the incident light is constant, from a stable light source, and that there is no relative motion between the components of the experimental configuration, i.e., everything is in a certain state of static equilibrium. The term "static light scattering" is often used to describe these techniques. Although the intensity of incident light (I_0) can be maintained at a constant level and the instrument can be stiffened, particles in the scattering volume are in constant motion coming from different sources. Motion can arise from random translational motions or thermal rotation (Brownian motion), forced motion introduced by an electric flux or field, or even motion resulting from bioactivity, such as the mobility of bacteria particles in water.

Any motion of the particles will cause changes, fluctuations or jumps, in the intensity of the scattering which can be fast or slow, depending on the nature of the motion and the type of particle. In any dynamic light scattering experiment except photon migration spectroscopy, the

intensity of the incident light is constant and the relative positions of the instrument components remain unchanged. The source of the intensity variation actually results from the motion of the particles, which causes changes in the relative positions between the particles, the light source, and the detector, and between the particles themselves, if there is more than one in the scattering volume. Thus, detecting variations in intensity can provide information about particle motions, and particle characteristics can be revealed from a different aspect than from a time-mediated measurement of intensity.

Other technologies that use light scattering to characterize particles are listed below:

- *Static Light Scattering* - measurement of absolute scattering intensity

- *Focused Beam Reflectance* - is a method of measuring a single particle. A laser beam is collimated and focused at one point. A mechanical device rotates the beam in a circular path. As the focal point intersects a particle, the particle scatters light back into a probe that transmits this scattering back to a photodetector, generating an electrical impulse. The duration and frequency of the pulse are indications of the length of the particles intersecting the beam and the number of particles.

- Time-of-Flight (TOF) measurement - *In particle size analyses using the TOF method, high-pressure* air transports predispersed particles through a converging nozzle. The particles are accelerated by shell flow at near-supersonic speeds. Particles of different masses will be accelerated differently. Two laser beams separated by a known distance detect individual particles when particles pass through the two beams consecutively. As particles pass through the beam, they scatter light that is collected and converted into electrical signals by two photomultiplier tubes. One tube detects light as the particle passes through the first beam, and the other tube detects scattered light as the particle passes through the second beam. Using the cross-correlation technique, the time difference between the light pulses detected at the two detectors indicates the time of flight, which is related to a certain particle size.

- *Time-of-Transition (TOT) measurement* - this technology is similar to focused beam reflectance in that it uses a rotating beam to scan a suspension of diluted air or liquid in which particles are presented and intercepted by the beam. The widths of the optical pulse represent the cable lengths of the particles intercepting the beam.

Turbidimetry - in a turbidity measurement, a spectrophotometer is used to measure the attenuation of light as a function of wavelength as it passes through a sample. In turbidity measurements, the refractive index as a function of wavelength is the variable used in size analyses.

- *Back Scattering measurement* - backward scatter detection can be achieved either using a CCD camera to record backward scattering images or by a PMT mounted on a translation stage to record angular scattering patterns, from which an intensity distribution is analyzed. Various fiber optic probes consisting of both illuminating and receiving fibers are used to measure the intensity of scattering at a certain angle. The intensity of light scattered backwards from individual particles follows the same theories previously described when the scattering angle is usually

greater than 165° . However, when direct scattering from samples in pipelines or reactors is detected, the particle concentration is usually much higher than what is required in single particle scattering. Multiple scattering is then always the dominant phenomenon, and interaction with particles is also another predominant factor. Therefore, direct measurement of particle size is not a trivial task. In both settings (using a CCD camera or fiber probes), particle size information can only be obtained indirectly, and apparent size values can be calibrated or correlated with actual values measured in diluted suspensions.

- *Phase Doppler Anemometry (PDA)* - Phase Doppler anemometry or phase Doppler analysis were proposed several decades ago, based on flow measurement technology - laser Doppler velocimetry. PDA is widely used in sizing spherical and homogeneous particles, such as liquid sprays, aerosols, air bubbles in liquid or other spherical particles.

4. DLS equipment

The measurement configuration used for DLS is shown in figure 2 and is similar with the configuration used to study static light scattering. The laser beam has a size of up to 1/10 mm, is focused on the center of the sample to be measured, and the photons scattered by the scattering centers are detected by a photodetector, sensitive and fast enough to be able to detect photons on their own. The angle θ represents the angle at which the sensor is placed relative to the direction of the LASER beam.

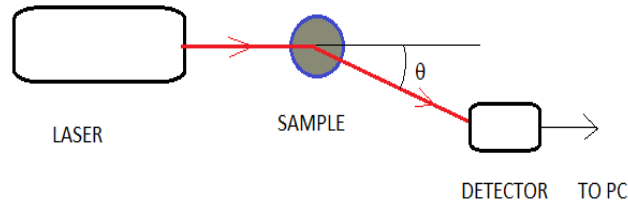


Figure 2: Hardware configuration for DLS measurement.

The data processing system, shown in figure 3, comprises the photodetector together with the signal preamplifier, analogue digital converter, digital data processing unit and result display system. Each series of photons detected by the photodetector produces a variable electrical signal. This signal is then processed by a preamplifier and sent to an analogue-to-digital conversion and data processing system.



Figure 3: Block diagram of signal processing system

A point detector, placed at a point at any position on the interference image (see figure 4), will record fluctuations in intensity. Lows and maximums will pass through it and we will thus obtain a time series (an analog signal, variable in amplitude and time).

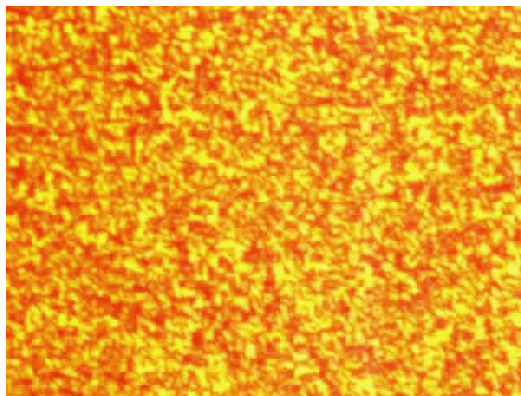


Figure 4: Projected image obtained using a 2 µm burnt clay suspension

In figure 5 we have a 15 second sequence of a recorded series placing the detector at a certain angle θ and we can see the evolution over time of the light intensity detected by the photodetector.

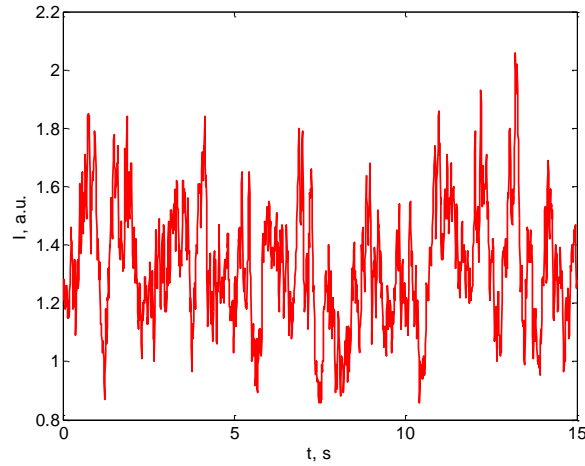


Figure 5: Time evolution of light detected by optical sensor

The analog signal is to be transformed by an analog-to-digital converter into a digital signal that will then be processed by a computing system. The obtained time series (in digital form) will be processed using the Fourier transform, thus obtaining the power density spectrum, whose shape depends on several parameters. By analyzing this spectrum, we obtain information about the particle size of the suspension used.

The particles in the sample under measurement, due to Brownian motion, are constantly in a rotational and translational motion, which creates fluctuations in the dielectric constant of the medium. Particulate matter can be regarded as secondary light sources. If the incident light is coherent, the secondary light waves emitted by these sources are also coherent, therefore they interfere, both constructively and destructively, leading to a boiling speckles aspect of the interference field. The fluctuation in the intensity of scattered light at a point is the result of the phase change of scattered light. The faster the particles move in the fluid, the faster the fluctuations in measured intensity. We also intuitively note that because of Brownian motion, smaller particles move faster than larger particles. This can be seen in the Einstein-Stokes relationship:

$$D = \frac{k_B T}{3\pi\eta d} \quad (11)$$

Where: D - diffusion coefficient - indicates how fast particles diffuse, k_B - Boltzmann's constant, η - solvent viscosity coefficient, T - sample temperature, d - particle diameter.

The method applied uses time series recorded with a data acquisition system, which then calculates the spectral power density. The spectral power density is then phytized using the Lorentz function described in equation (12), using a nonlinear least squares minimization procedure, thus determining the appropriate parameters of the function:

$$S(f) = a_0 \frac{a_1}{(2\pi f)^2 + a_1^2} \quad (12)$$

Where: f is the frequency of the spectrum and a_0 and a_1 are parameters. The parameter a_0 scales the shape of the function to arrive at the initial form, and a_1 is directly related to the size of the particles, according to the equation:

$$R = \frac{2\pi k_B T K^2}{6\pi\eta a_1} \quad (13)$$

Where: k_B - Boltzmann's constant, η - solvent viscosity coefficient, T - sample temperature, K - scattering vector modulus, as described in the equation:

$$K = \frac{4\pi n}{\lambda} \sin\left(\frac{\theta}{2}\right) \quad (14)$$

Where: n - refractive index of the solvent, λ - wavelength of LASER radiation, θ - scattering angle.

The procedure involves finding the two parameters, and then, based on parameter a_1 , estimating the average particle size using equation (13). The diagram of the DLS reference procedure is shown in figure 6:

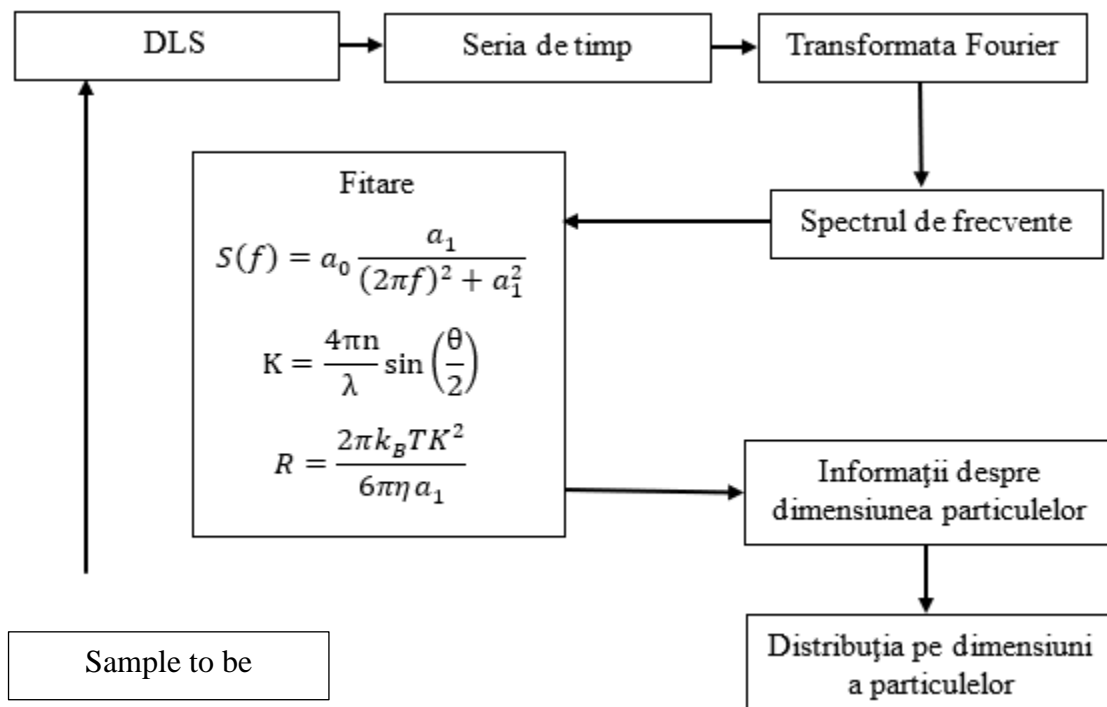


Figure 6: DLS reference procedure diagram

5. Optical sensors

Photodetectors are electronic components or devices that can convert the energy of electromagnetic radiation (both invisible and visible) into electrical energy, relying on the absorption in the solid body of electromagnetic radiation and radiative recombination in semiconductor of charge carriers.

Photodiodes are semiconductor elements containing a p-type region and an n-type region in contact in a passage zone called the p-n junction. The structure and symbol are shown in figure 7:

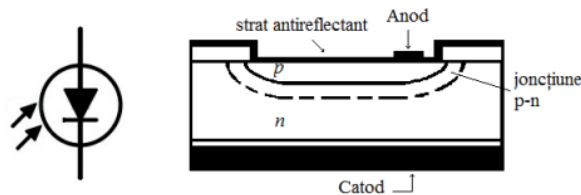


Figure 7: Symbol and structure of a photodiode

In the absence of an external field, free charge carriers in regions p and n have disordered motion, electrons diffuse to region p and gaps to region n. At the meeting between electron and hole, recombination occurs, causing a decrease in the concentration of electrons in the n zone and holes in the p-zone. This phenomenon causes the n region to become electropositive, behaving like a true electrical source. In the junction arises an internal electric field directed from region n to region p, which limits the migration of carriers.

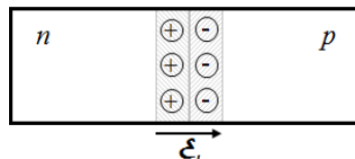


Figure 8: Recombination phenomenon

Under the action of radiation, electron-hole pairs are generated in the semiconductor if the energy of the incident photons is greater than the forbidden bandwidth. The charge carriers generated by light diffuse to the p-n junction where they are separated under the action of the internal electric field: the holes are directed to the p region, and the electrons to the n region. Thus, with illumination, electrons accumulate in the n region, resulting in an additional negative charge, and in the p region a positive charge occurs. At the terminals of the p-n junction, a photoelectromotive voltage arises that polarizes the junction directly.

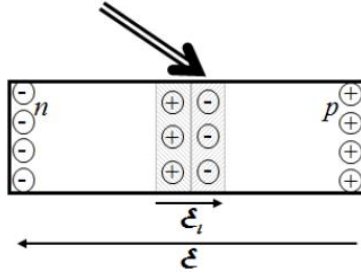


Figure 9: The occurrence of photoelectromotive voltage at the junction terminals under the action of radiation

If the circuit closes by a charge resistance, then excess electrons from region n will move through the outer circuit to region p, giving rise to an electric current due to illumination of the p–n junction. The occurrence of an electromotive voltage in a p-n junction when it is illuminated is called the photovoltaic effect. Through this effect, the direct conversion of light energy into electrical energy is achieved.

Neglecting the phenomena of recombination-generation in the dam layer, the characteristic equation of the illuminated p-n junction is:

$$I = I_{SC} + I_s \left(e^{\frac{eU}{kT}} - 1 \right) \quad (15)$$

where: U -voltage at terminals; I_{SC} - short circuit current (proportional to luminous flux); I_s - reverse saturation current.

The following figure shows the volt-ampere characteristics of a photodiode at different illumination values.

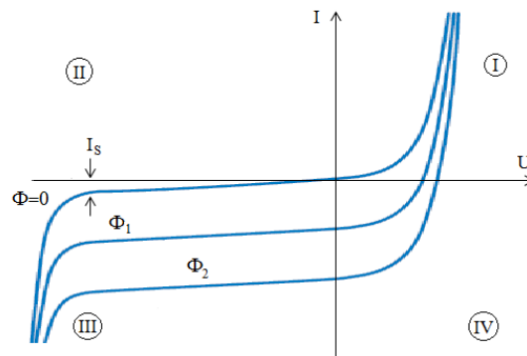


Figure 10: V/A characteristics of a photodiode under the influence of different illumination values

In quadrant III, the photocurrent is proportional to the incident luminous flux on the photosensitive surface, being quasi-independent of the reverse voltage value until close to the breakthrough voltage (which can be on the order of tens of volts). The photodiode can be used as a photodetector when operating in reverse polarization mode.

Quantum efficiency is the ability of a photodiode to convert light energy into electrical energy, expressed as a percentage, represents its quantum efficiency (Q.E.).

$$\eta = \frac{r_e}{r_p} = \frac{\text{number of collected electrons ca } I_p/\text{sec.}}{\text{number of incident photons/sec.}} \quad (16)$$

It depends on λ , through absorption coefficient, layer thickness, doping, geometry, etc. When operating under ideal conditions of reflectance, crystal structure, and internal strength, a high-quality silicon photodiode with an optimal design may be able to approach an 80% Q.E.

The sensitivity of photodiodes R_λ is defined as the ratio of radiant energy (in watts), P , incidence of light on the photodiode and photocurrent output in amperes I_p . It is expressed as the absolute response in amperes per watt. Radiant energy is usually expressed as watts/cm², and photodiode current as amperes/cm². The term cm² cancels and we are left with amperes/watt (A/W).

$$R_\lambda = \frac{I_p}{P} \quad (A/W) \quad (17)$$

Because: $h\nu = \text{photon energy}$, $P = r_p h\nu$

where: $r_p = \text{photon flux} = P/h\nu = \text{number of photons/sec}$

Typical features of photodetectors:

Photodetector	Wavelength (nm)	Responsivity (A/W)	Dark Current (nA)	Rise Time (ns)
Germanium	1000–1500	0.70	1000	1–2
InGaAs APD	1310–1550	0.80	30	0.100
InGaAs PIN	1310–1550	0.85	0.5–1.0	0.005–5
Silicone PIN	850–950	0.6–0.8	10	0.070
Silicone PN	550–850	0.41–0.7	1–5	5–10

Equivalent operating circuit

A photodiode behaves as a photocontrolled current source in parallel with a semiconductor diode. The circuit model is given in the figure below.

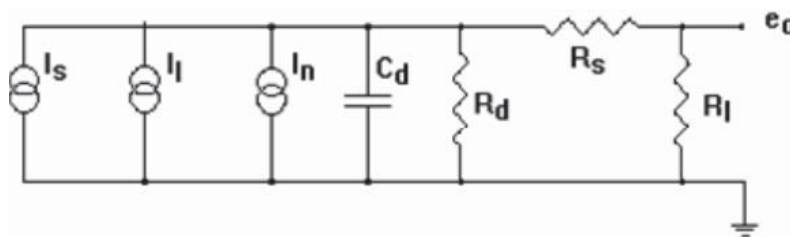


Figure 11: Equivalent circuit of a photodiode

$$e_0 = (I_s + I_l + I_n) \frac{R_l R_d}{R_d + R_l + R_s} \quad (18)$$

where: I_s = signal current
 R_d = parallel resistance of photodiode
 I_l = reverse saturation current
 R_s = series resistance of photodiode
 I_n = noise current
 R_l = load resistance
 C_d = diode junction capacitance

$$BW_{PD} = 1/[2\pi(\tau_{tr} + \tau_{RC})] \quad (19)$$

where τ_{tr} is the transit time of the photocarriers to the terminals and τ_{RC} is the time constant imposed by the capacitance of the active region, C_d , and the load resistance, R_s .

Basically, a photodiode is a current generator. The junction capacity of the photodiode depends on the depth of the emptying layer and, therefore, on the reverse bias voltage. The value of parallel resistance R_d is usually large (megaohms). The resistance of the R_s series is low. The effect of the load resistance value R_l on the current/voltage characteristics is shown in figure 12:

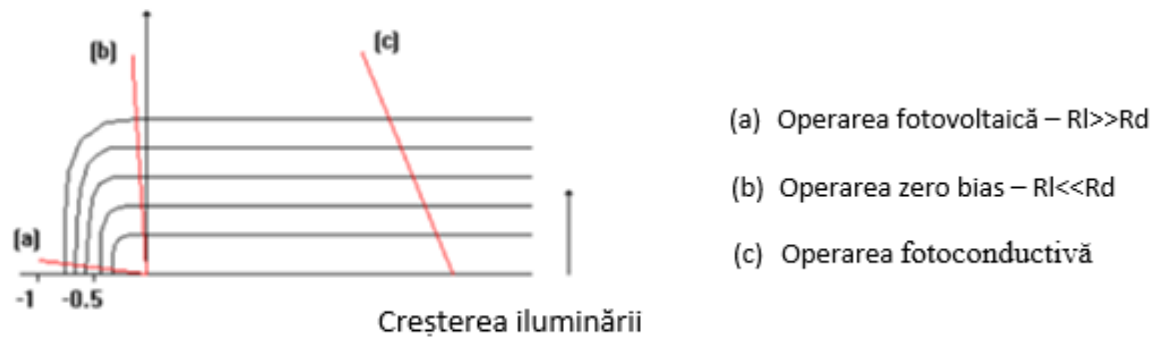


Figure 12: Effect of load resistance, R_s , on I/U characteristic

6. Optical detector. Functional blocks, practical design, and realization

For the development of the detection and processing system of the light signal obtained from the phenomenon of light scattering by suspended particles in the analyzed fluid, we considered several parameters:

- power, wavelength, coherence, and stability of the LASER emitter.
- sensitivity and reaction speed of the photodetector.
- the dark noise of the photodetector.
- gain factor, bandwidth, and preamplifier noise.
- rejection of abandoned signals, both in the emission chain and in the signal detection and processing chain.
- sampling rate of the analogue-to-digital conversion system.
- computing capabilities of the data-processing system.

The circuit chosen for the optical detector consists of an operational amplifier configured as a transimpedance amplifier. It amplifies the incident light-dependent current of a PIN photodiode. For this detector, the photodiode will operate in photoconductive mode: exposure to light will cause a reverse current through the photodiode. The diode is connected in such a way that this current causes the output voltage of the operational amplifier to increase.

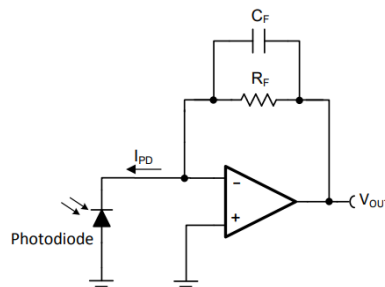


Figure 13: Connecting a photodiode to a transimpedance amplifier

$$V_{OUT} = I_{PD}R_F \quad (20)$$

The reaction capacitor, C_F , is designed to maintain the stability of the circuit. This capacitor compensates for the capacitance of the photodiode at the inverting input of the operational amplifier.

In the absence of current through the photodiode, the output of the amplifier will try to stabilize at the voltage applied to the noninverting input. If the noninverting input were connected to potential 0, the output voltage would ideally be 0 V. However, the output voltage can never reach 0V since this is also the value of the negative supply. Therefore, the output of the operational amplifier will "saturate" around the negative power supply. This condition should be avoided, as it could delay the amplifier's response to an input signal. To avoid saturation, a resistive divider from the positive feed is used to polarize the noninverting input of the amplifier above the negative power level.

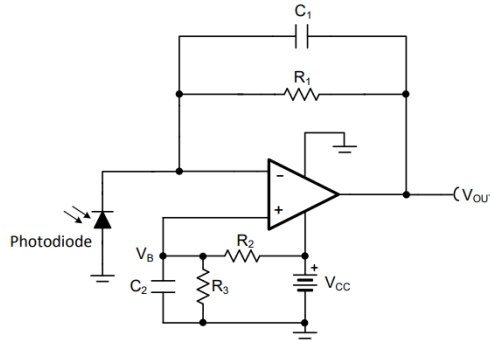


Figure 14: Application of bias voltage to noninverting input to avoid output saturation

The form of the output voltage, considering the application of a bias voltage on the noninverting input, is as follows:

$$V_{OUT} = i_{PD}R_1 + V_B = i_{PD}R_1 + V_{CC} \frac{R_3}{R_3+R_2} \quad (21)$$

The photodiode chosen for the detector is a PIN diode with code SFH213. The operating spectral range (400 nm – 1100nm), spectral sensitivity and response speed (switching time approx. 5 ns) correspond to the requirements required for the photodiode to be used in the photo detector.

For the chosen scheme, the diode will be reverse-polarized and therefore the C_J junction capacitance will be used for stability calculations when V_R = 0. Also, due to minimal reverse polarization, the effects of dark current on the amplifier output can be neglected. The chosen diode has the following parameters necessary for calculations:

Parasitic diode capacitance: C_J = 11pF (V_R = 0)

Illumination reverse current: I_{PD} = 90μA (E_e = 1mW/cm²)

The operational amplifier chosen for practical realization is OPA320, in the SOT-23 capsule, a precision operational amplifier made in CMOS technology. The main characteristics behind this choice were low noise, high response speed, high frequency bandwidth and power supply from a single power line.

Some of the features of this operational amplifier:

- Low offset voltage: 150 μV (Maximum)
- High Common Mode Rejection (CMRR): 114 dB
- Low bias current: 0.9 pA (Maximum)
- Low noise: 7 nV/ $\sqrt{\text{Hz}}$ at 10 kHz
- High bandwidth: 20 MHz
- Growth rate: 10 V/ μs
- Current consumption: 1.45 mA
- Single wide-range supply voltage: 1.8 V to 5.5 V

The OPA320 amplifier is a high-speed, precision circuit suitable for low-power and single-power applications. Low noise (7 nV/ $\sqrt{\text{Hz}}$), low output impedance, flat frequency characteristics and high linearity across the entire frequency range ensure very good performance for the signal processing stages that precede analog-to-digital converters.

The main requirements for the construction of the circuit were as follows:

- single supply voltage - 5V; - Current consumed - < 1.5mA; - Input current (photodiode) - 0 - 90 μA ; - Output voltage - 100mV - 4.9V; - Amplification - about 90dB.

The electronic diagram of the detector is shown in figure 15. The calculation of the circuit gain will be made considering the requirements related to the output voltage range and the maximum current through the photodiode:

$$\frac{V_{OUT(MAX)} - V_{OUT(MIN)}}{I_{IN(MAX)}} = R_1 \rightarrow \frac{4.9V - 0.1V}{90\mu A} = 53333.3\Omega \rightarrow R_1 = 53.6k\Omega \quad (22)$$

The feedback capacitor together with the feedback resistance will establish a peak in the frequency response of the amplifier. This peak we set at 1MHz:

$$f_P = \frac{1}{2\pi C_1 R_1} \quad (23)$$

The calculation of the capacitor in the feedback circuit will be made to ensure the linearity of the circuit up to a frequency of 1Mhz:

$$C_1 \leq \frac{1}{2\pi R_1 f_P} \leq \frac{1}{2\pi(53.6k\Omega)(1MHz)} \leq 2.97pF \rightarrow 2.7pF \quad (24)$$

The bias network will be calculated from the minimum requirement 0.1V for the output signal. Thus, for $V_B = 100\text{mV}$, if the current through the photodiode will be 0, the output will not be saturated at 0, but will be maintained at a value of 100mV:

$$V_B = V_{CC} \frac{R_3}{R_2 + R_3} \rightarrow 0.1 = 5 \frac{R_3}{R_2 + R_3} \rightarrow 0.02 = \frac{R_3}{R_2 + R_3} \rightarrow R_2 = 49R_3 \quad (25)$$

Choosing $R_2 = 13.7k\Omega$, we get $R_3 = 280\Omega$

The capacitor C_2 is placed parallel to resistor R_3 to reduce the influence of power supply noise on the signal at the amplifier output. Selecting a $1\mu\text{F}$ value for C_2 produces a cut-off frequency of:

$$f_P = \frac{1}{2\pi C_2(R_2//R_3)} = \frac{1}{2\pi * 1\mu\text{F} * (13.7\text{k}\Omega // 280\Omega)} = 580.028\text{Hz} \quad (26)$$

The obtained value is high enough to stop any disturbances coming from the power supply from passing to the amplifier output.

The operational amplifier of choice, OPA320, meets and sometimes exceeds the requirements of this detector. The passive components used in practical implementation shall be within a tolerance of 1 %.

When making the printed wiring, it was considered that the power circuits were disconnected to the ground path and that no loops appeared that could lead to the appearance of parasitic signals.

The entire circuit was inserted into a metal box equipped with photodiode hole, 5 V DC connector and signal output connector.

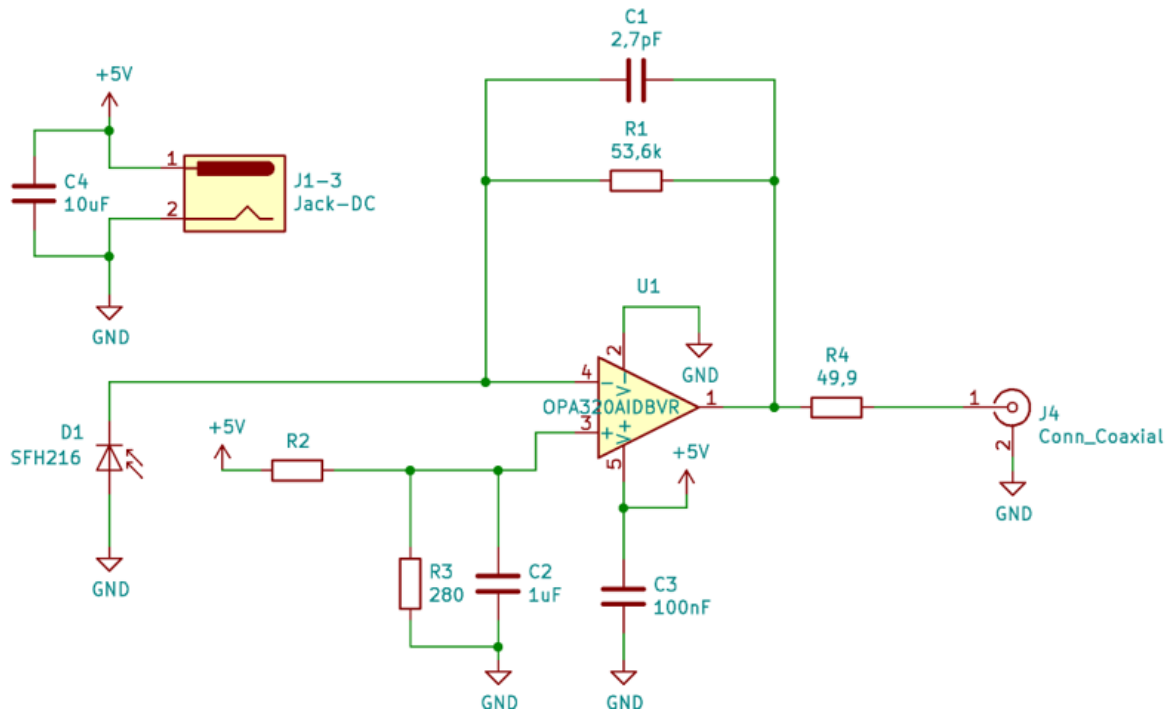


Figure 15: Optical detector - electronic diagram

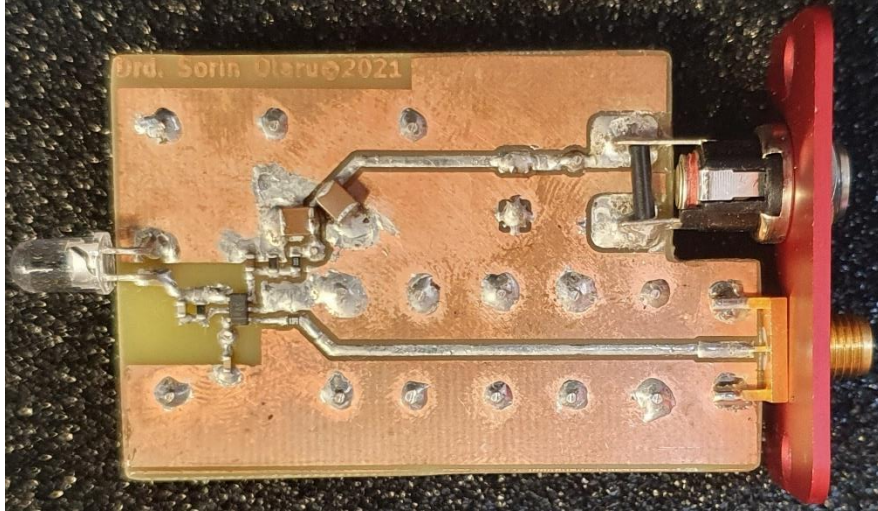


Figure 16: Optical detector - printed circuit board equipped

7. – Amplification and linearity measurements

Laboratory measurements were made using the following equipment:

- LeCroy Teledine oscilloscope with 400 MHz frequency band.
- Hameg signal generator 10 MHz.
- LeCroy current and voltage probes.
- Power supply Rhode & Schwartz.
- LED HLMP-NG07 high frequency – for stimulation of optical detector.

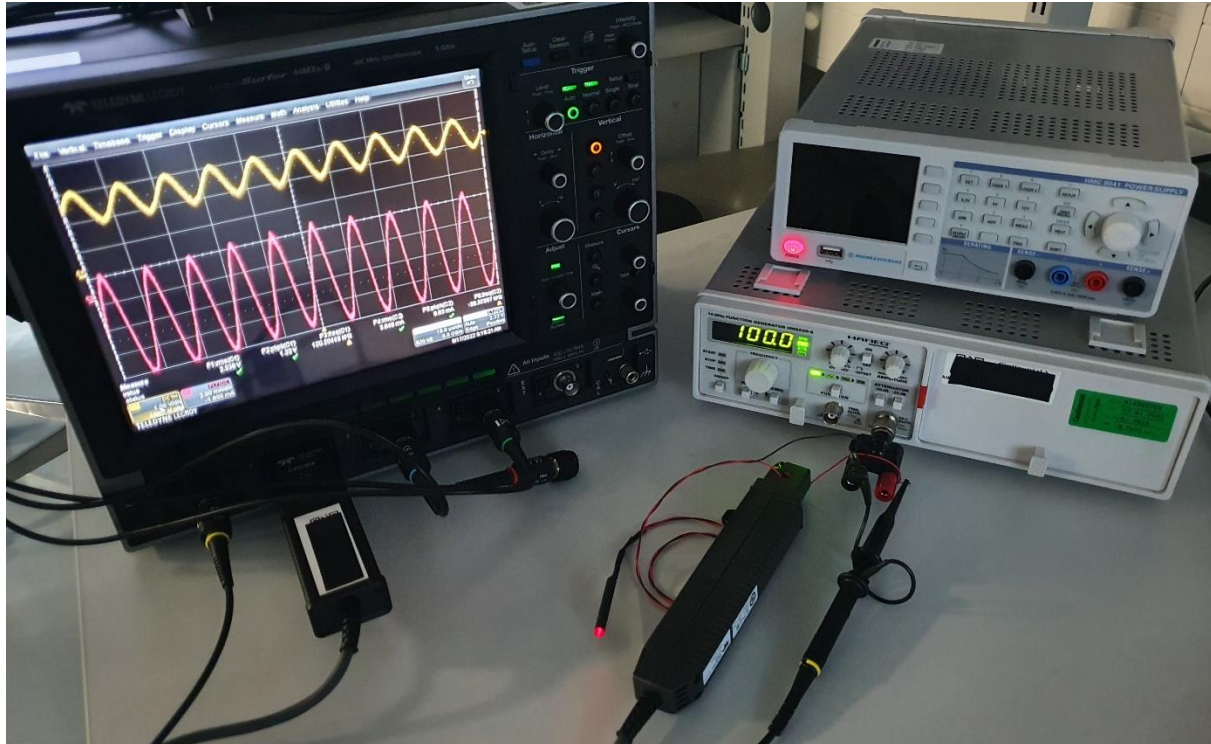


Figure 18: Measuring equipment used for linearity measurements

The supply voltage used to supply the LED emitter and the current through it were monitored and kept constant throughout the tests.

Measurements were made for frequency values from 50 Hz to 5 MHz. Most measurements were made in the range of interest 50 Hz – 100 kHz.

In the images below (figures 19 – 22) you can see oscilloscope captures for some of the measurements. In the table (figure 23) we have the values of the LED current and the value of the output voltage from the photo detector. The graph shows the evolution of the output signal as a function of frequency. You can also see the evolution of current through emitting diodes, also correlated with frequency change.

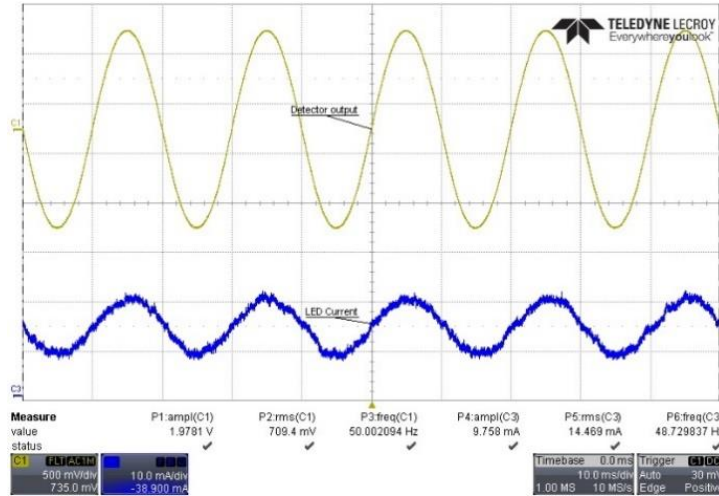


Figure 19: Output voltage as a function of input signal strength @ $f = 50$ Hz

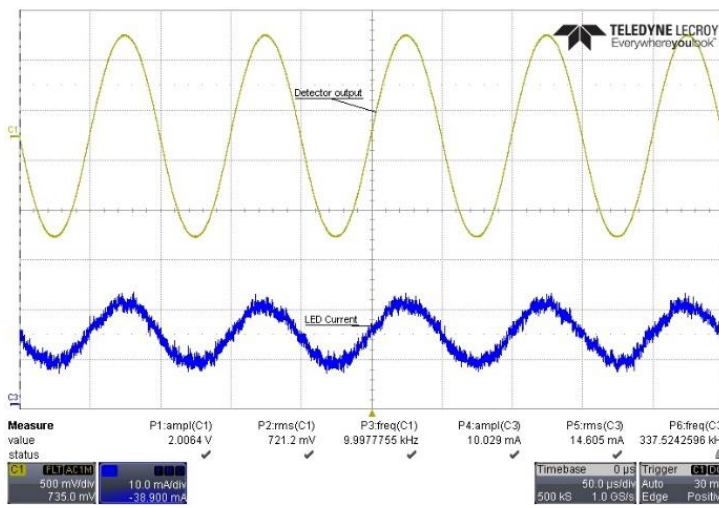


Figure 20: Output voltage as a function of input signal strength @ $f = 10$ kHz

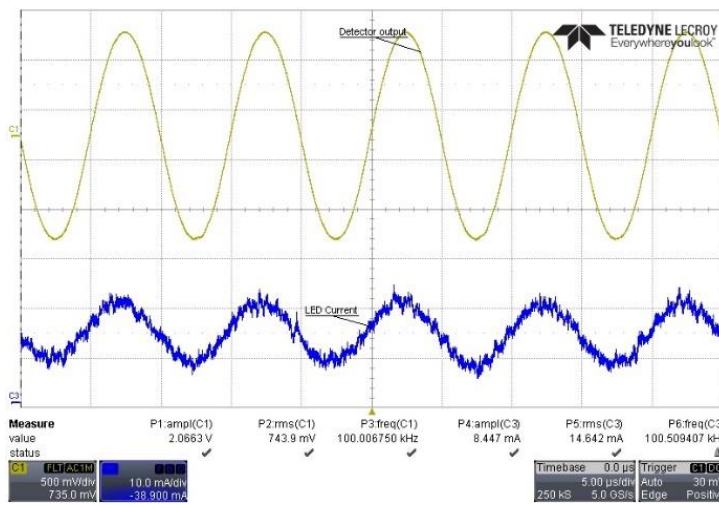


Figure 21: Output voltage as a function of input signal strength @ $f = 100$ kHz

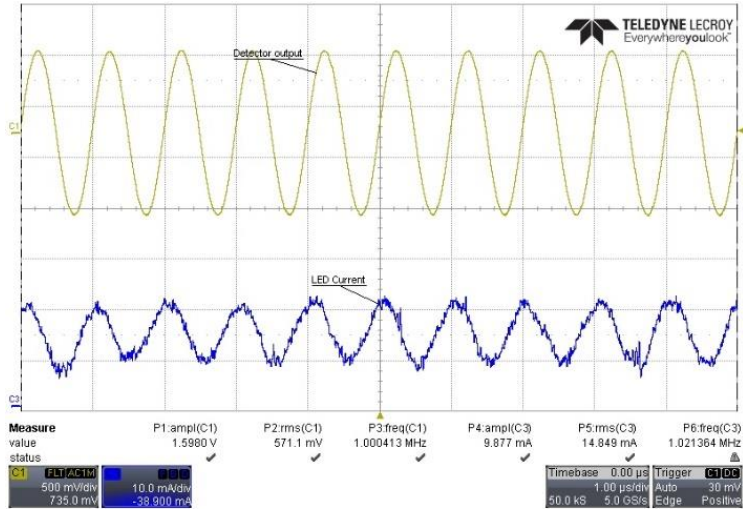


Figure 22: Output voltage as a function of input signal strength @ $f = 1$ MHz

Frequency [kHz]	LED current [mA RMS]	Output voltage [mV RMS]
0.05	14.4	709.4
0.1	14.7	712.1
0.5	14.4	716.9
1	14.7	719.8
5	15	718.8
10	14.6	721.2
20	14.9	725.6
30	14.9	729.5
40	15	731.2
50	14.8	731.6
60	14.2	739.7
70	16	744.5
80	14.4	746.2
90	15.4	747.1
100	14.6	743.9
1000	14.8	571.1
1500	15.5	446.3
2000	15.3	339.9
3000	15.1	198.3
4000	15.5	117
5000	14.9	74.8

Figure 23: LED current and corresponding output voltage of photo detector

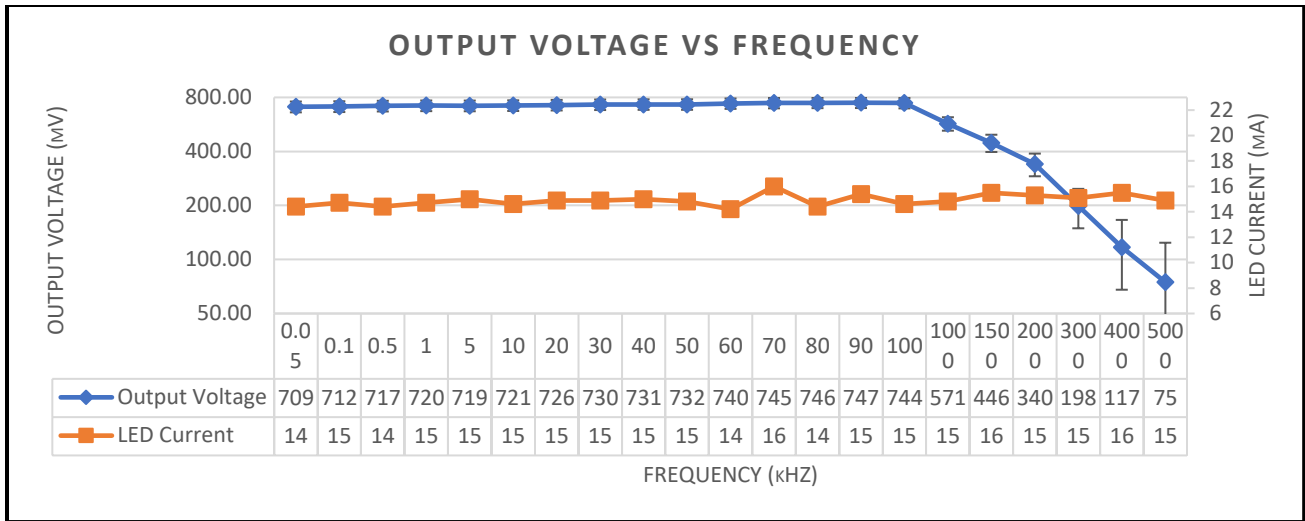


Figure 24: Output voltage as a function of frequency (constant input stimulation):

The circuit was also simulated in the range 10Hz – 5MHz using the TINA application. The equivalent diagram used in the simulation tool is shown in figure 25. Instead of the photodiode, a constant amplitude, variable frequency signal was injected into the range specified for simulation (figures 26).

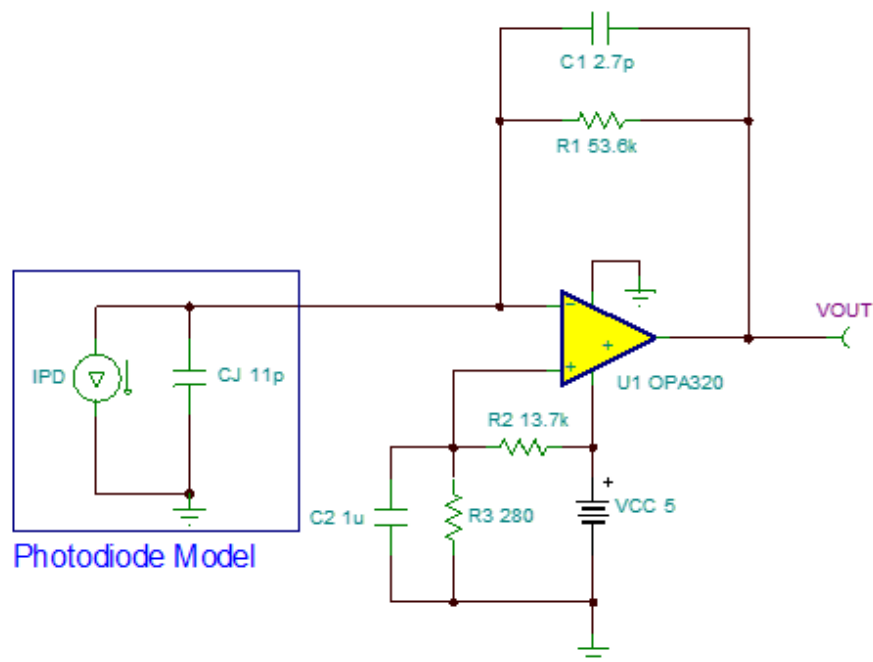


Figure 25: Simulated equivalent diagram

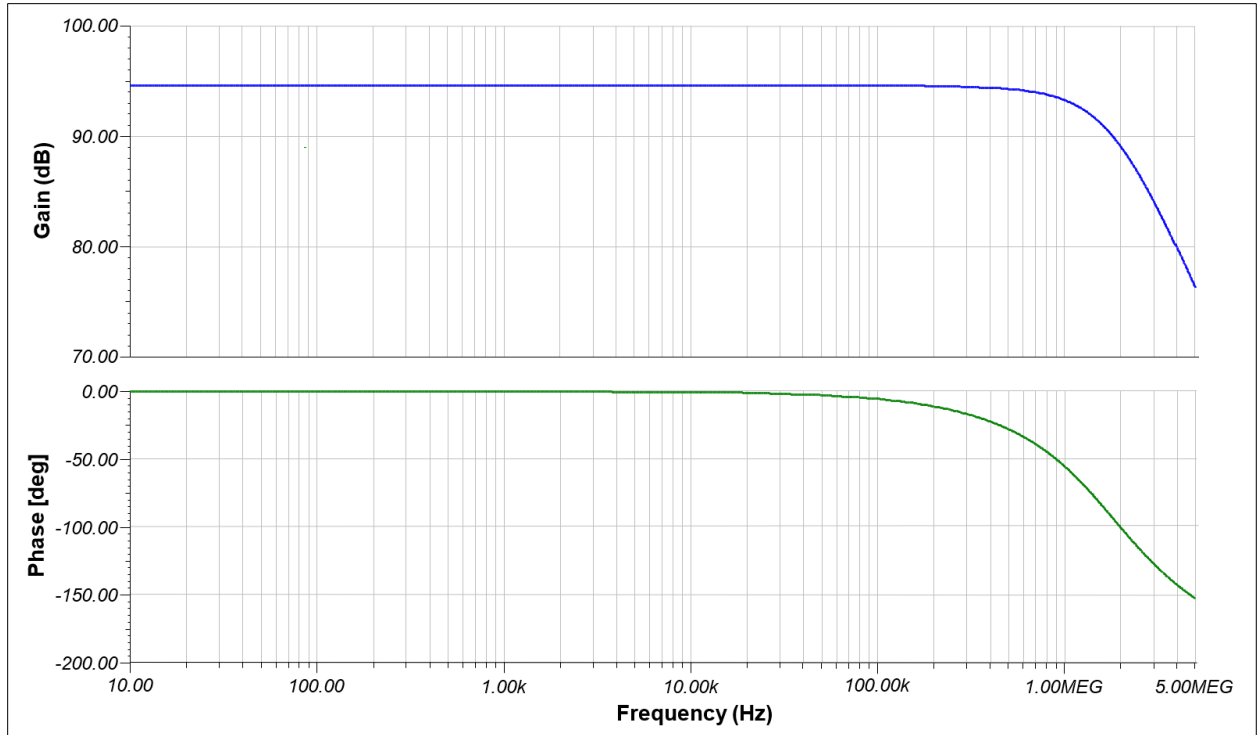


Figure 26: Bode diagram 10Hz – 5 MHz:

8. Particulate measurements using the stepwise filter filtration method

As the first step in the manufacturing process of electronic modules, we have particle cleaning of metal housings used for certain categories of electronic processing units.

This step is necessary to prevent the possibility of contamination of electronic wafers with conductive particles. Also, as part of the process of continuous product improvement and cost efficiency, it is necessary to find out the density of particles and their distribution by size categories. The data obtained will be used to streamline the cleaning process and improve the production process of metal housings.

The analysis was made to the solvent used by metal casing washing plants. It was processed through a series of membranes with through-hole sizes of different values. The analysis was performed using a filtration plant and a chemical recess (figure 27).

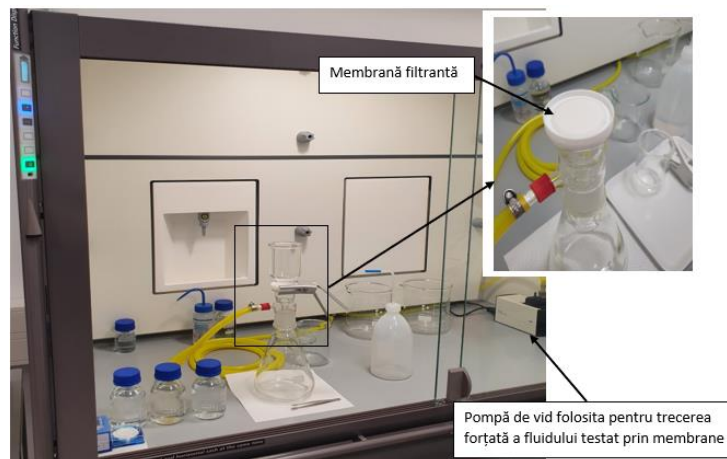


Figure 27: Laboratory equipment used for measurements

We used membranes with the following pass sizes: 15 μm , 5 μm , 1 μm , 0.8 μm . The diameter of the filter membranes is 47 mm and the useful filtration surface has a diameter of 45 mm.

The steps in this analysis were as follows:

- taking the sample to be measured. From the amount of solvent used, take 1000 ml.
- cleaning the equipment – with a 0.8 μm filter mounted in the particulate retention area, clean the installation using the cleaning solvent until the filter no longer retains any particles. In the first phase, the evaluation was done by direct observation and then by examination under a microscope.
- calibration of the measuring system – we use a membrane of 0.8 μm and a quantity of 250 ml of pure solvent, identical to that used in the parts washing installation. The quantity of fluid is passed through the filtration system and the membrane is kept as a standard to confirm the degree of cleanliness of the installation.

- mount the membrane with 15µm through-holes and pass 250ml of the sample to be measured. The fluid resulting from passing through the filter will constitute the test for the next step.

- Mount the membrane with 5µm through-holes and pass 250ml of the sample to be measured. The fluid resulting from passing through the filter will constitute the test for the next step.

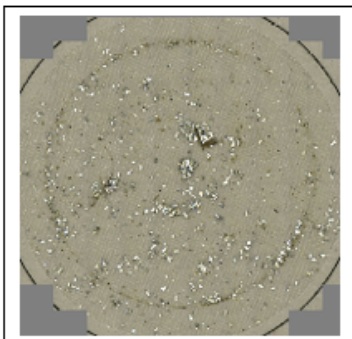
- Mount the membrane with 1µm through-holes and pass 250ml of the sample to be measured. The fluid resulting from passing through the filter will constitute the test for the next step.

- mount the membrane with 0,8µm through-holes and pass a quantity of 250ml of the sample to be measured. The fluid resulting from passing through the filter will constitute the test for the next step.

- The next steps consist of drying the membranes for 20 minutes in an oven with the temperature set at 100°C and then cooling and dehumidification in a controlled atmosphere enclosure for 2 hours. The temperature is set at 21°C and the humidity at 33% RH.

After completing all membrane preparation procedures, scanning them using a digital microscope and interpreting the data follows.

General information			
Analyse Operator:	Sorin Olaru	Extraction Operator:	Sorin Olaru
Product Specifications:	TST N 002 02.45-001 Cleanliness-Inspection ECU	Inspection (Procedure):	ISO16232
Test object			
Part designation:	NA	Component size:	250 cm ² per part
Article code:	Downclean solvent	Amount of parts on filter:	1
Sample No:	1	Supplier:	ALL
Extraction			
Extraction method:	Filtration	Extraction liquid:	HAKU 1025-810-1
Amount extraction liquid [ml]:	250	Filter type:	Nylonmembrane 15 µm
Microscopic analysis			
Scale:	5.9 µm/Pxl	Evaluated diameter [mm]:	42.0
Evaluation according to ISO 16232 / VDA 19.1			
	Length [µm]	Width [µm]	
Largest metallic shiny particle	3737	2724	
Second largest metallic shiny particle	3020	1475	
Largest non-metallic shiny particle	1958	393	
Second largest non-metallic shiny particle	1934	1297	
Widest metallic shiny particles	3737	2724	
Second widest metallic shiny particles	2726	1765	
Widest non-metallic shiny particles	1934	1297	
Second widest non-metallic shiny particles	1599	508	
Longest stretched fiber	11208	76	
Second longest stretched fiber	1778	33	
Inspection result:			



Filter occupancy [%]: 8.12

Figure 28: 15µm filter - Nylonmembrane 15µm

General information			
Analyse Operator:	Sorin Olaru	Extraction Operator:	Sorin Olaru
Product Specifications:	TST N 002 02.45-001 Cleanliness-Inspection ECU	Inspection (Procedure):	ISO16232
Test object			
Part designation:	NA	Component size:	250 cm ² per part
Article code:	Downclean solvent	Amount of parts on filter:	1
Sample No:	1	Supplier:	ALL
Extraction			
Extraction method:	Filtration	Extraction liquid:	HAKU 1025-810-1
Amount extraction liquid [ml]:	250	Filter type:	Multilayer Pall 5 µm
Microscopic analysis			
Scale:	5.9 µm/Pxl	Evaluated diameter [mm]:	42.0
Evaluation according to ISO 16232 / VDA 19.1			
	Length [µm]	Width [µm]	
Largest metallic shiny particle	465	193	
Second largest metallic shiny particle	87	17	
Largest non-metallic shiny particle	144	21	
Second largest non-metallic shiny particle	141	34	
Widest metallic shiny particles	465	193	
Second widest metallic shiny particles	53	37	
Widest non-metallic shiny particles	92	67	
Second widest non-metallic shiny particles	55	48	
Longest stretched fiber	1590	17	
Second longest stretched fiber	818	26	
Inspection result:			

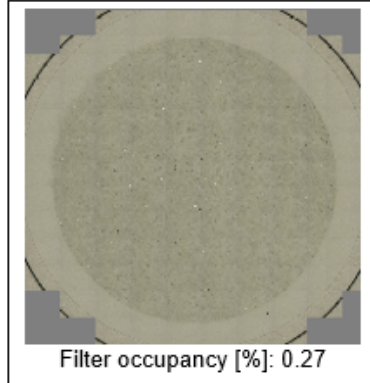


Figure 29: 5µm filter - Multilayer Pall 5µm

General information			
Analyse Operator:	Sorin Olaru	Extraction Operator:	Sorin Olaru
Product Specifications:	TST N 002 02.45-001 Cleanliness-Inspection ECU	Inspection (Procedure):	ISO16232
Test object			
Part designation:	NA	Component size:	250 cm ² per part
Article code:	Downclean solvent	Amount of parts on filter:	1
Sample No:	1	Supplier:	ALL
Extraction			
Extraction method:	Filtration	Extraction liquid:	HAKU 1025-810-1
Amount extraction liquid [ml]:	250	Filter type:	Nylonmembrane 1µm
Microscopic analysis			
Scale:	1.5 µm/Pxl	Evaluated diameter [mm]:	40.0
Evaluation according to ISO 16232 / VDA 19.1			
	Length [µm]	Width [µm]	
Largest metallic shiny particle	96	11	
Second largest metallic shiny particle	53	23	
Largest non-metallic shiny particle	163	18	
Second largest non-metallic shiny particle	99	15	
Widest metallic shiny particles	53	23	
Second widest metallic shiny particles	31	23	
Widest non-metallic shiny particles	67	46	
Second widest non-metallic shiny particles	31	28	
Longest stretched fiber	3587	33	
Second longest stretched fiber	1073	23	
Inspection result:			

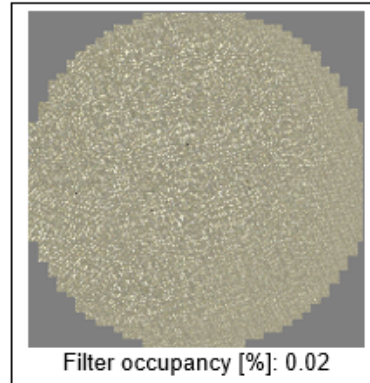


Figure 30: 1µm filter – Nylonmembrane 1µm

General information			
Analyse Operator:	Sorin Olaru	Extraction Operator:	Sorin Olaru
Product Specifications:	TST N 002 02.45-001 Cleanliness-Inspection ECU	Inspection (Procedure):	ISO16232
Test object			
Part designation:	NA	Component size:	250 cm ² per part
Article code:	Downclean solvent	Amount of parts on filter:	1
Sample No:	1	Supplier:	ALL
Extraction			
Extraction method:	Filtration	Extraction liquid:	HAKU 1025-810-1
Amount extraction liquid [ml]:	250	Filter type:	Cellulose membrane 0.8µm
Microscopic analysis			
Scale:	1.5 µm/Pxl	Evaluated diameter [mm]:	40.0
Evaluation according to ISO 16232 / VDA 19.1			
	Length [µm]	Width [µm]	
Largest metallic shiny particle	70	14	
Second largest metallic shiny particle	51	26	
Largest non-metallic shiny particle	176	19	
Second largest non-metallic shiny particle	160	31	
Widest metallic shiny particles	39	28	
Second widest metallic shiny particles	33	28	
Widest non-metallic shiny particles	53	43	
Second widest non-metallic shiny particles	130	42	
Longest stretched fiber	573	8	
Second longest stretched fiber	523	28	
Inspection result:			

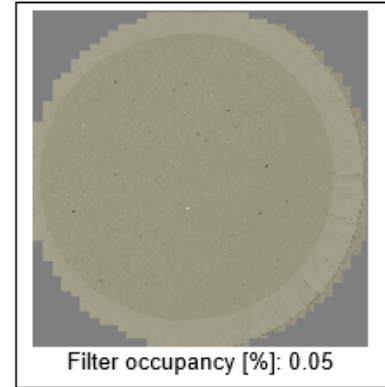


Figure 31: 0.8µm filter – Cellulose membrane 0.8µm

To analyze the particles found in the parts cleaning solution, the stepwise filtration method was used. The particles identified ranged from a few tens of µm to thousands of µm as equivalent hydrodynamic volume.

The method is sufficient for profiling particles in this size area, but inefficient for particles of a few µm or nm size.

Also, the procedure is a long one, both for the running phase of the tests and for the measurement and interpretation of the data.

9. Measurement of particulate size in air (smoke and aerosols) using DLS technique

The detection, measurement, and analysis of particulate matter in the air is of great importance in areas such as environmental monitoring, health, pollution, combustion engines, automotive, fire detection, meteorology, and many others. Particulate matter in air is also called aerosols or suspended particles in air.

The size of suspended particles in air is up to $100\mu\text{m}$. Larger particles are not suspended, and their fall rate is usually greater than 1m/s .

There are several methods and sensors for analyzing particles suspended in the air. Mechanical methods consist in the mechanical collection of suspended particles from the air. This can be done either with the help of filters or with the help of a centrifuge. If filters are used, a fan forces air through a filter that collects particles from the air. The particles attached to the filter are examined using a microscope and very detailed information about the particles is obtained. This method is simple and straightforward, but at the same time laborious and time consuming. A faster and simplified mechanical method is to use selective filters with holes of decreasing size. A version of this method is the gravimetric method: Weigh a clean filter, then filter through it a large amount of air with particles. After filtering the large volume of air, the filter is weighed again. The difference in mass divided by the volume of filtered air is the mass concentration of the particles.

Another method of mechanical collection of suspended particles is to use a centrifuge. The force applied to a particle inside a centrifuge is thousands of times greater than its weight in normal gravity. For example, a $20\mu\text{m}$ particle falls 1 cm/s into air with a normal gravity of 1g . The same particle will have a velocity of 32cm/s in a centrifuge with 1000g or 1m/s in a large centrifuge with 10000g . Small particles that do not settle in normal gravity can be separated in a centrifuge. Then, particles attached to the circumference of the centrifuge can be analyzed using a microscope.

Mechanical methods are precise and accurate but are limited to laboratory measurements. They are not suitable for automated analysis or high-volume measurements or continuous air monitoring.

A different method is to ionize particles suspended in air. In the middle of the last century, the first smoke sensor with a radioisotope and an ionization chamber appeared. Such a sensor includes a very small amount ($0.3\mu\text{g}$) of Americium 241 that ionizes air molecules inside the ionization chamber. Americium 241 is preferred because its radiation is 1% gamma and 99% alpha, which has a high ionization power and can also be easily shielded. A voltage is applied between two electrodes in the chamber and the current between the electrodes is monitored. If smoke particles are inside the chamber, ions will adhere to them, and the current between the electrodes will change. Thus, smoke can be detected. Such sensors are not very reliable and are less and less used. Sometimes they are used in conjunction with other types of sensors, mostly because ionization sensors are more sensitive to small particles, unlike optical sensors that are sensitive to large particles. Ionization of air molecules can be done by Corona discharge instead of radioactivity.

The signal generated by an ionization smoke sensor depends on both the size and density of the particles, therefore none of them can be measured. The size could be measured if the particle density is known and after calibration with particles of known size. But these conditions cannot be achieved for a commercial sensor.

Optical sensors are most used for detecting and analyzing particles in the air. A light source illuminates a volume of air. The particles inside the illuminated volume scatter light. A light sensor measures either transmitted light or scattered light, and the electrical signal generated is amplified and analyzed to obtain information about the particles.

Sensors that count particles have a light source (LED or laser) and a lens that focuses the light beam according to the size of a particle. A thin stream of particulate air circulates between the light source and a photodetector in the region where the light is focused. Each particle passing between the light source and the photodetector will produce a pulse in the signal from the photodetector. The pulses are counted and the particle density can be calculated. Some detectors have additional electronics and software to analyze each pulse and estimate the size of each particle, but the accuracy is very low and they can only distinguish between dust and smoke.

Optical smoke sensors are installed in most public buildings and some homes. An LED and photodiode are placed inside an optical camera. They are arranged in such a way that neither direct nor reflected light from the LED can reach the photodetector. Airborne suspended particles entering the chamber scatter light, and a certain amount of scattered light is detected by the photodiode.

Diffused light sensors are cheap, small, and reliable. They are used to detect smoke or dust but cannot measure particle parameters. The signal level generated by the photodetector is highly dependent on the density, size, shape, color of the particles, therefore none of these parameters can be measured separately.

Nephelometers are used to accurately measure the concentration of suspended particles in a fluid. These are basically optical sensors with light scattered at an angle of 90° . Although they are expensive and sensitive, they cannot directly determine the concentration of particles. As mentioned earlier, scattered light depends on the concentration, size, shape, and color of the particles. Size, shape and colour must be known in advance to measure concentration. A nephelometer must be calibrated for a known particle before measuring its concentration in the atmosphere.

The most advanced nephelometers can measure the dimensional distribution of particles. This goal can be achieved by the SLS (Static Light Scattering) method. Nephelometers manufactured by Air Photon or TSI measure scattered light for three wavelengths and scattering angles from 7° to 170° . Data obtained from three photomultipliers (for three wavelengths) are processed to obtain the size distribution and density of the particles. These instruments are expensive, heavy (on the order of kilograms) and include many moving parts and sensitive optical components.

Extinction optical sensors measure the intensity of direct light from an LED or laser. When particles are between the light source and the detector, the light intensity on the photodetector is lower. Most sensors have an optical camera, and the distance between the light source and the photodetector is a few centimeters. Alternatively, the distance is several meters. In this case, a laser beam targets a photodetector that is several meters away. Thus, the monitored area is much larger, but false detections can occur more often.

The DLS (Dynamic Light Scattering) method has been used for a long time (about 60 years) to measure the size of particles suspended in liquid. The DLS method requires several basic components: a photodetector and a light source that must be monochromatic and coherent (thus a laser), a data acquisition system and a computing system. The light parameter measured by DLS is the frequency of scattered light, while all other methods need the intensity of scattered light. The monochromatic light scattered by particles creates an interference image on the photodetector. The intensity of light on the photodetector is the result of random phases of light coming from illuminated particles. But particles move continuously due to Brownian motion, therefore, the phase and intensity of light on the photodetector are variable. The speed of particles in Brownian motion depends on the size of the particles. The frequency of the signal generated by the photodetector is processed by a computer and the particle size can be calculated.

Overview of DLS data processing procedure

The DLS procedure uses a coherent beam of light focused on particles suspended in a solvent, usually a liquid solvent. The light scattered by particles is also coherent, therefore an interference image is produced, and the interference intensity of light can be measured by a detector and recorded using a DAS (digital acquisition system) data acquisition system. The recorded data are called time series in DLS and are processed in a fairly simple way to obtain the average diameter of suspended particles. There are several approaches, each based on certain approximations and assumptions, that can lead to calculating the size distribution of particles, such as the CONTIN algorithms or Maximum Entropy (as described in this paper).

The following is presented a method of assessing the size of suspended particles in air (aerosols) using DLS. DLS is a simple procedure that can be used to process time series generated by airborne particles, which can produce the average size of nano and microparticles, making it an advanced sensor and at the same time a simple, low-cost device.

A diagram of the basic DLS installation is shown in figure 32. The light source, which must be coherent, can be either a He-Ne laser or a laser diode. The typical wavelength for these light sources is 633 nm. The scattering angle θ is variable, as will be explained below. The lateral displacement can be adjusted to have the appropriate dispersion angle. The samples consist of micro and nanoparticles suspended in the air. The distance D between sample and detector can be adjusted so that the average speckle size corresponds to the detector size (as much as possible).

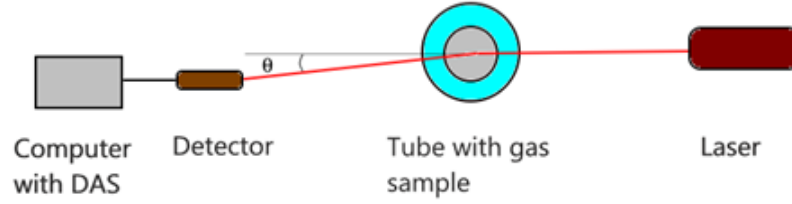


Figure 32: Experimental configuration used for measurements

DLS time series consist of values recorded by the DAS with a given sampling frequency f . This means that the light intensity is recorded at time intervals $\Delta t = 1/f$. As stated in, the width of the autocorrelation of the intensity time series is proportional to the diffusion coefficient, which depends on the diameter of the diffusion centers (SC hereafter).

The frequency spectrum (FS -frequency spectrum) is related to the autocorrelation of a process, as proved by the Khinchin–Kolmogorov theorem. An alternative version is described below.

FS can be described analytically using the Lorentzian line $S(f)$:

$$S(f) = a_0 \frac{a_1}{(2\pi f)^2 + a_1^2} \quad (27)$$

Two parameters, a_0 and a_1 , are included in the Lorentzian line $S(f)$. The parameter values in equation (27) shall be determined so that the Lorentzian line $S(f)$ best describes FS calculated with the recorded time series. The parameters can be determined using a minimization procedure. Then the radius can be calculated using equations (28) and (29):

$$R = \frac{2k_B T q^2}{6\pi\eta a_1} \quad (28)$$

where q is the modulus of the scattering vector:

$$q = \frac{4\pi n}{\lambda} \sin \frac{\theta}{2} \quad (29)$$

In equations (28) and (29) R is the mean radius of suspended particles, k_B is Boltzmann's constant, T is the absolute solvent temperature, η is the dynamic viscosity of the solvent, n is the refractive index of the solvent, λ is the wavelength of the laser beam, and θ is the recording angle.

Equation (27) describes the FS form of the DLS time series of particles in a solvent with a certain angle of dispersion at a certain temperature. To plot the expected shape of ideal FS, a_1 can be calculated by returning to equation (28).

If scattering centers (SC) are suspended in water, the parameters are: temperature = 20°C, $n = 1.33$ and $\eta = 1.02 \cdot 10^{-3}$ daP. If particles are suspended in air at 100°C, the parameters are approximately two orders of magnitude smaller: $n=1$ and $\eta=2.1704 \cdot 10^{-5}$ daP. This affects parameter a_1 for the same particle radius. Equation (28) shows that, for the same radius R , a_1 is inversely proportional to η , therefore, a decrease in η will increase the parameter a_1 accordingly, so that the rotation point (frequency) in the graph FS as a function of frequency, as in figures 33

and 34, will be shifted to higher frequencies. For successful processing of such a DLS time series, higher sampling rates are required for data acquisition, therefore, more expensive equipment for light detection and data acquisition, thus falling outside the scope of the targeted device, which is a relatively low-cost sensor using ordinary electronic equipment, that is, manufactured in large series. Such equipment is used in audio devices for personal computers: audio preamplifiers and sound cards, be it internal cards or external USB sound cards.

The typical dispersion angle for most DLS experiments is 90° , mainly because, with respect to FS, the plateau of the logarithmic-logarithmic graph extends over a wider frequency range, and therefore the evaluation of the rotation point, i.e., parameter a_1 , is more accurate. The frequency spectrum, simulated for the diameters mentioned above, is illustrated in Fig. 33.

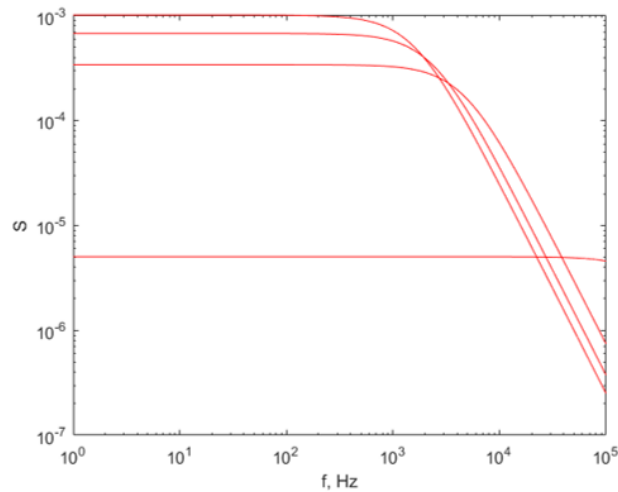


Figure 33: FS simulated for particle diameters in the set: 5, 338, 672 and 1000nm at a scattering angle of 90° , with air at 100°C as solvent. The lower curve represents FS for the smallest diameter, 5nm, while the upper curve is for the largest diameter, 1000nm. The sampling rate was 200 ks/s.

Fig. 33 shows that the rotation point (frequency) on the lowest curve, corresponding to the diameter SC of 5nm, is beyond the highest limit of the frequency range in the graph, therefore the least squares adjustment method will not identify a_1 in equation (27). Consequently, the correct radius of smaller nanoparticles cannot be determined using the parameters mentioned above.

Graphs for smaller scattering angles in, such as 5° , suggest that DLS is possible in air for relatively low sampling frequencies of 100 ks/s. Although this sampling rate may seem small, such sampling rates are not easy to achieve with relatively inexpensive electronic devices such as those defined above.

If we consider the low-cost electronics class, we consider sampling rates of up to 44 ks/s. In addition, we can imagine using a sound card for PC or laptop, which is a DAS of good quality and low cost. A sampling rate of 44 ks/s is common for purchasing high-fidelity audio with a frequency of up to 22 kHz. Regular sound cards have an analog-to-digital converter with a resolution of up to 32 bits. However, sound cards should be used with some caution, if there is no

spectral attenuation from the detector to the input, since sometimes filters are applied in sound cards or computers for recording sound.

Figure 34 shows the simulated frequency spectrum for the same set of diameters mentioned above, assuming the same sampling rate of 200 ks/s recorded at a scattering angle of 10° .

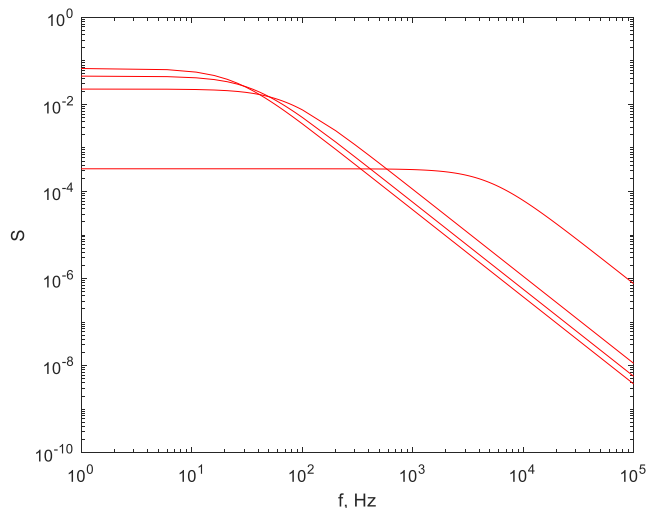


Figure 34: FS simulated for the set of diameters at a dispersion angle of 10° . The bottom curve represents FS for the smallest diameter, 5nm, while the top curve is for the largest diameter, 1000nm. The sampling rate was 200 ks/s.

If the scattering angle is reduced to 10° , we note that it might be possible to successfully match the Lorentzian line to the calculated FS, thus finding a_l and the diameter of the particles, since the point of rotation of the line is now in the frequency range of the spectrum calculated using the fast Fourier transform (FFT) algorithm, which is 0-22 kHz, if a sampling rate of 44 ks/s is used. In addition, the points of rotation of the lines corresponding to the different particle diameters are clearly separated from each other in figure 34, so that adjustment by the method of least squares can be applied with reasonable accuracy.

The experimental configuration that was used to record the time series for DLS for airborne particles is illustrated in Figure 32. The coherent light source was a He-Ne laser with an ordinary wavelength of 633 nm. The scattering angle θ was chosen to be 10° , as decided during the FS simulations. The detector consisted of a silicon PIN photodiode SFH213 and a transimpedance amplifier as described in the previous chapter. The acquisition and recording were performed using a PC's sound card at a sampling rate of 44100 samples/s. The amplitudes were subsequently extracted and the DLS time series were processed by the data processing procedure as described below.

The viscosity of air depends largely on temperature; therefore, the temperature was measured using a digital thermometer, with the temperature sensor in the transparent tube, just above the laser beam. The dynamic viscosity coefficient η was calculated using the Sutherland correlation, which expresses its dependence on the absolute temperature of an ideal gas, based on the kinetic theory of ideal gases.

Time series were recorded for 30 s each time. FS was calculated using the Fast Fourier Transform (FFT) algorithm, and only 220 = 1,048,576 data were used, since the FFT algorithm uses a 2n data number. If more data is provided, the function fills the rest of the values with 0 to match the number 2(n+1), with the direct consequence of indicating a much larger amplitude for very low frequencies than the real one.

An FS of one of the recorded DLS time series is illustrated in figure 36. We can see that the tipping point is within the frequency range, and this allows the evaluation of a_1 and, subsequently, the diameter of the particles. The FS of the recorded time series contains noise that is visible on diagrams in the form of peaks around frequencies, with amplitudes much higher than those in the rest of the spectrum. Therefore, filtering is required. After calculating the FS, a filtering procedure was applied, which eliminated a bandwidth of 2.5Hz centered on 50Hz and higher harmonics, since 50Hz is the frequency of the electrical network and noise with this frequency is present in all recordings.

In addition, normalisation of FS was also applied, which is required for DLS on gas-suspended particles. The intensity of scattered light depends largely on both the numerical density of the particles and the size of the particles, by means of the scattering parameter g , therefore, different samples will produce FS with considerably different amplitudes. For finding parameters a_0 and a_1 , a procedure for minimizing the least squares is used, that is, finding the parameters of the Lorentzian line that best describes FS calculated on DLS time series. The adjustment procedure stops, among other criteria, when any of the parameters changes by less than a predetermined quantity. The adjustment is more accurate when both parameters have comparable values or at least the same order of magnitude. The parameter a_1 is in the range from tens to thousands, therefore, the normalization of FS is carried out by multiplying all amplitudes in one set in FS so that the height of the plateau is of the order of magnitude several thousand.

After filtering the FS spectrum and normalizing it, the Lorentzian line was adjusted to the spectrum, a_0 and a_1 were determined, followed by calculating the particle radius using equation (28) and diameters.

Error calculation

First, we need to check whether the fluid flowing around the object, SC in this paper, is in Stokes mode. The autocorrelation of a DLS, or FS, time series depends on the diffusion coefficient. If the fluid flowing around the object is in the Stokes regime, the resistance is described by the Stokes equation and equation (28) is correct. The Knudsen number describes the fluid flow regime.

Going further, if equation (28) is perfectly accurate, we can obtain the relative error when evaluating the radius R of the particle by substituting equation (29) into equation (28) and writing the logarithm of R as a first step, in equation (30).

$$R = \frac{16\pi k_B n^2}{\eta a_1 \lambda^2} T \sin^2 \frac{\theta}{2} \quad (30)$$

If we consider that all constants are grouped as a single factor, the differential of that factor will be null. If we consider that the quantities we measured, and which were therefore sources of error, were the thermodynamic temperature T and the angle of measurement θ , the logarithm of R is:

$$\ln(R) = \ln \frac{16\pi k_B n^2}{\eta a_1 \lambda^2} + \ln T + 2 \ln \left(\sin \frac{\theta}{2} \right) \quad (31)$$

If we differentiate equation (31) and consider dT and $d\theta$ to be the experimental errors in measuring these quantities, under the assumption of the worst case in which errors are summed, we obtain equation (32):

$$\varepsilon_R = \frac{\Delta R}{R} = 0 + \frac{\Delta T}{T} + \frac{1}{\tan \left(\frac{\theta}{2} \right)} \Delta \theta \quad (32)$$

Considering an error for temperature of 3K, the distance between detector and tube, and the diameter of the transparent tube, we found that the relative error was quite large, up to 31%. Although the error is quite large, it is still consistent with the purpose of describing a simple procedure for setting up and processing data for a sensor. Figure 35 shows a column describing the error when assessing particle diameter using our experimental setup and data processing procedure, together with average diameters for samples used to test the procedure.

Try	a_1 [Hz]	Average diameter [nm]	Δd [nm]	K_n
Smoke from paper burning with flame	244.2	565	175	0.14
The wick of a wax candle, smoldering	1771.4	78	24	0.83
Nebuliser	410.0	336	104	0.19
Cigarette smoke	6166.0	22	7	3.0
Smoke from smouldering burning paper	9393.1	15	5	4.39

Figure 35: Samples analysed, parameter a_1 and average diameter.

Results

Several materials were ignited with different flame regimes to produce smoke and particles and were used as laser beam targets in the experimental configuration shown in figure 32. The samples that produced particles are shown in figure 35.

Figure 36 illustrates FS calculated for the DLS time series recorded on smoke from burning flame paper as a particle source, after filtering out network noise and harmonics and adjusting the Lorentzian line to FS. We note that noise frequencies of 50Hz have been eliminated. The red, continuous line represents the Lorentzian line, equation (27), drawn with the best match parameters, where a_1 was 244.2 Hz, corresponding to a larger average diameter of smoke particles of 565 nm.

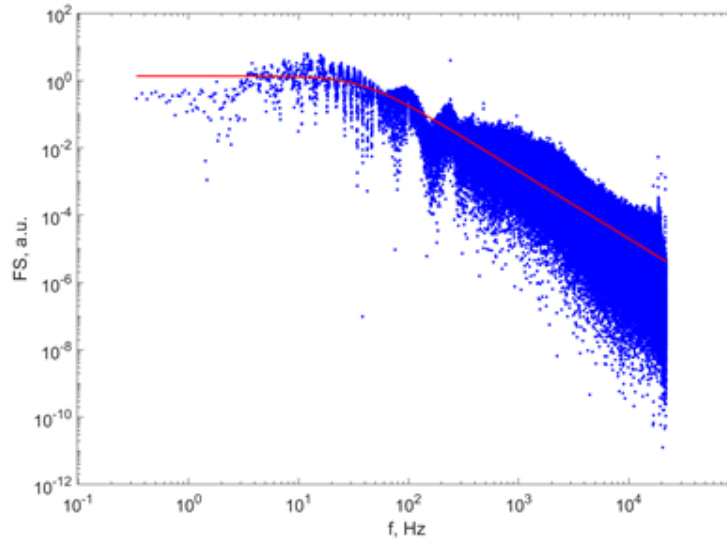


Figure 36: FS after filtration (blue dots) and Lorentzian line (continuous line) for particle in smoke from flame burnt paper

Figure 36 also shows that the line matches the calculated FS quite well, confirming that the approximation of having monodispersed particles in the sample is acceptable.

Figure 37 illustrates FS calculated for the DLS time series recorded on cigarette smoke, following the same data processing procedure after filtering network noise and harmonics, and after adjusting the Lorentzian line to FS. The red, continuous line represents the Lorentzian line, was drawn with the best match parameters, which, for this sample, a_1 was 6166.0Hz, which corresponds to an average diameter of particles in cigarette smoke of 22nm. We note that the approximation of the monodisperse dimensional distribution of particles holds true for this sample as well, since the line fits reasonably well with experimental FS.

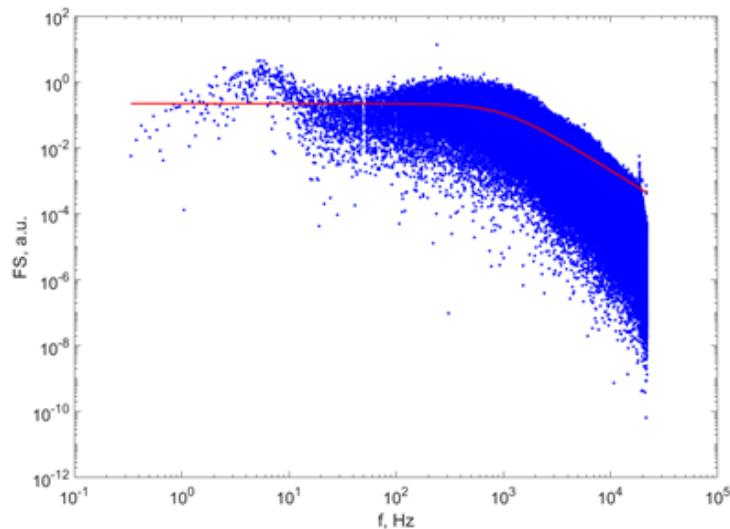


Figure 37: FS after filtration (blue dots) and Lorentzian line (continuous line) for cigarette smoke particle.

The same aspect of FS and the line adjusted to it can be observed on FS for DLS time series recorded on particles produced by a burning wax candle wick, where the average diameter was 78nm, and for particles produced by burning paper, where the calculated average diameter was 15nm.

So far, the samples that have been analyzed and presented indicate that DLS time series recorded for airborne particles as solvent, with a relatively low data acquisition rate, can be processed using the approximation that particles have a monodisperse or narrow dimensional distribution. The procedure should be tested on samples with a known wider particle size distribution and compare the results with the actual size distribution. One such source of airborne particles is a nebulizer that uses a small compressor to disperse medical solutions into aerosol particles. Figure 38 illustrated FS calculated for DLS time series recorded on water droplets in aerosols used as a sample, following the same data processing procedure. The red, continuous line represents the Lorentzian line, was drawn with the parameters of the best match, which, for this sample, a_1 was 410.0Hz, which corresponds to an average diameter of particles in aerosol droplets of 336nm. This time, aerosol droplets have a wider distribution, with a maximum diameter of 2.6 μ m. We note that the low-frequency part of FS does not appear to be a plateau, and that the entire FS appears to be a sum of FS recorded for one-dimensional particles. The adjustment indicated an average diameter of 336 nm.

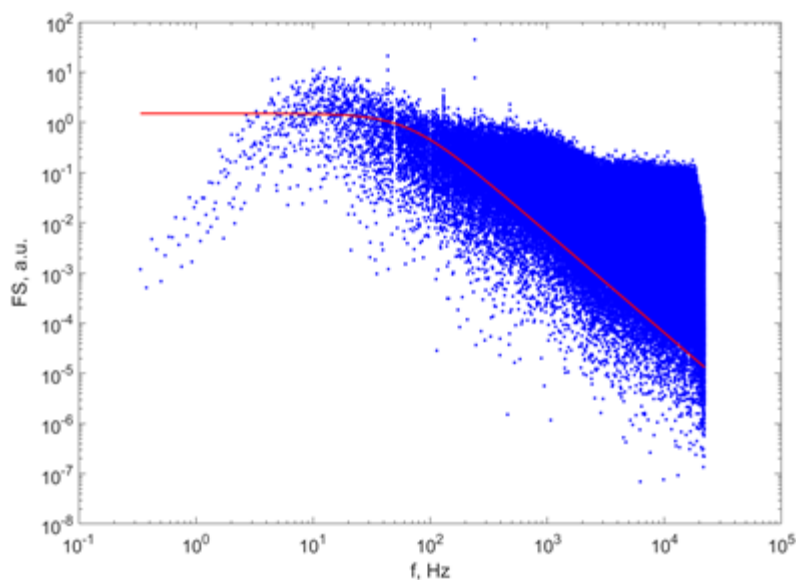


Figure 38: FS after filtration (blue dots) and Lorentzian line (continuous line) for airborne particles produced by a nebuliser.

The particle size assessed using this procedure is consistent with the generic particle size as reported in the technical literature, which states that petroleum smoke has a particle size between 0.03 - 1 μ m, tobacco smoke is between 0.01 - 4 μ m, petroleum smoke between 0.03 - 1 μ m and wood burned with flame between 0.2 - 3 μ m, which we assume is comparable to burnt paper.

10. Measurement of particle size in air using DLS technique on an aqueous suspension containing wind-borne Sahara dust particles

In the previous paragraph we showed that it is possible to characterize particles suspended in a gas if there is a sufficiently high concentration of particles so that the scattered signal is detectable and can be analyzed (the situation with smoke from various open or smoldering fire sources). If this condition is not met, the measurement procedure must be adjusted. In this paragraph the characterization of particles suspended in a gas, but in low concentration (dust particles for example), is presented. These particles from air were collected and concentrated by dilution in distilled water. Finally, we applied the DLS technique to characterize the particles in air, but analyzing an aqueous solution in which these particles were embedded.

In early April 2022, a cloud of Saharan dust moved over Romania, followed by rain containing dust particles (aerosols), which settled on objects. Dust aerosols are one of the major factors affecting the global climate system.

I saw this as a good opportunity to try characterizing wind-borne Saharan dust particles, and to compare the results with those published in the literature.

Atmospheric aerosols and their optical parameters are an important factor in models for estimating global climate change. Dust particles present in the atmosphere can have either a cooling or warming effect, depending on the layer altitude, single dispersion albedo, and base surface albedo. On surfaces with a surface albedo of more than 0.3, mineral aerosols usually heat the atmosphere. Over oceans, forests, and dark surfaces with surface albedos of less than 0.15, mineral aerosols have an atmosphere-cooling effect. For albedo values between 0.15 and 0.30, the effect depends on both size distribution and chemical composition. Consequently, the net radiative effect shows significant regional variations, which partly explains the difficulty of estimating the magnitude and type of effect (heating or cooling) of the radiative disturbance caused by dust particles.

Moreover, desert dust carried by air currents contributes heavily to air pollution, reducing air quality by increasing particulate matter concentrations, which affects human health by increasing mortality risk. The average annual temperature in the Sahara is more than 30 °C, making this region one of the hottest on Earth's surface. It stretches from the Atlantic Ocean to the Red Sea, between Sub-Saharan Africa in the south and Mediterranean North Africa in the north, making it the largest desert in the world. Sandstorms usually occur in conditions of very strong winds generated by the large difference in air density between hot and cold air masses. They usually occur in summer, but can also appear in spring, as in 2022.

References report that dust particle size and chemical composition have been analyzed by various methods. The size distribution of aerosols was found to contain most particles in the diameter range of 0.1–2.0µm.

The rain on the days when the dust cloud was over Romania (April 4-5) brought dust particles to the ground, which were deposited on surface objects. Because the cloud contained low

concentrations of Saharan dust, its main effect was to dirty car windshields and outside appliances, as well as house windows. Such deposits were taken on April 6 using a sterile bandage previously moistened in deionized water. The wet bandages were soaked in deionized water and squeezed, releasing water containing the suspended dust particles. All operations were performed using sterile latex gloves. It should be noted here that the air naturally contains a small amount of local dust produced by air currents that exist in any region. Since it rained for a relatively long time during the study period, for about two weeks before the dust cloud reached Romania, most of the local dust was transported to the ground by rain. After several days of rain, objects on the ground such as cars - especially those with dark paint, where dust is more visible - showed no signs of dust accumulation once the rain stopped. This suggests that there was minimal or no local dust in the air. The dust that was transported to the ground by rain after Saharan dust reached the territory was therefore mostly Saharan dust, with a very small amount of local dust. Next, we call this dust "Saharan dust."

The suspension containing the Saharan dust particles was kept at +2°C in a refrigerator until it was analysed using the combination of DLS and sedimentation. The fluid obtained as described, the aqueous suspension, was shaken for 5 minutes using a magnetic shaker, and a small amount of 1.5 ml was transferred to the transparent tube of the DLS device.

It should be noted that Saharan dust was lifted into the atmosphere by warm air currents, transported first over the Atlantic Ocean, then over the western part of Europe and, finally, over the territory of Romania. With this in mind, there was enough time for the giant dust particles to be eliminated naturally.

Overview of DLS data processing procedure

As mentioned earlier, the DLS technique used for characterization evaluates the hydrodynamic diameter of particles suspended in a liquid solvent.

Experimentally, particles suspended in a liquid solvent are the target of the laser beam. The coherent incident light is scattered by each particle in the beam area in all directions, thus producing the distant interference field. Since each location of the interference field contains information relating to the motion of each particle that scattered light, it is possible to evaluate information on the diffusion properties of the particles and, among them, the size of the particles. This is achieved by recording a time series from a remote field location, most often at a scattering angle of 90°, and analyzing it to evaluate the diffusion coefficient; Then, from there, the size distribution of the particles or the average hydrodynamic diameter of the suspended particles.

The rollup method is one of the first methods used to analyze DLS time series and is based on the autocorrelation function of a single-mode distribution. This method does not accurately describe multimodal systems. To solve this problem, analysis by the method of least negative squares (NNLS – non negative least squares) was introduced. Other methods, which can be considered variants of NNLS, are CONTAIN and maximum entropy algorithms.

There are also newer alternatives to DLS time series processing, based on the use of artificial neural networks (ANNs). Using a medium frequency spectrum of scattered light intensity as input for an ANN estimates the average diameter of particulate matter for particles with a diameter of less than 350 nm. ANN-based study and laboratory analyses extended the particle size characterization range to 6000 nm. ANN-based procedures reported in the literature were hundreds or thousands of times faster than procedures based on adjusting an analytical function, either on the frequency spectrum or on the autocorrelation of DLS time series.

Despite being very fast, these ANN-based alternatives give no indication of the accuracy of the result, relative to the accuracy of the single-mode approximation on which they are based. As seen in DLS analysis on particles in air as solvent, the accuracy is not considerable, the main cause being the small angle and the relatively large error of angle measurement caused by the diameter of the transparent tube containing the sample. In addition, the concentration of particles required to perform DLS measurements on particles in the air is quite high, as is the concentration of particles in smoke; therefore, this alternative is not suitable for a very low concentration of particles in the air produced by the Saharan dust cloud that has reached eastern Europe.

To overcome the uncertainty that could be generated by using an ANN-based alternative and to overcome the possible problem of not having a sufficiently high particle concentration, a DLS data series processing procedure was used that uses an adjustment of an analytical function to experimental data. In addition, a brief presentation of the procedure aimed to simplify the experimental configuration as much as possible and make it more flexible is presented below. The experimental configuration is shown in figure 39.

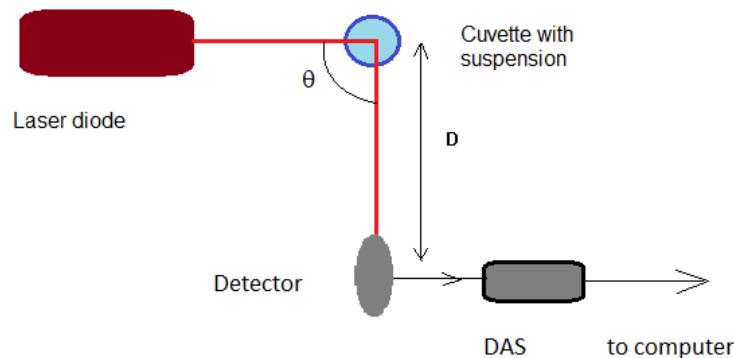


Figure 39: Diagram of the experimental assembly, with top view. The dark blue circle represents the bowl and the light blue disc inside represents the aqueous suspension.

The installation consists of a laser diode, a cylindrical cell containing the suspension, a digital acquisition system (DAS), an optical detector and a computer for recording time series. The wavelength of the light beam of a laser diode is 635nm. The laser diode operated in continuous mode at a power of 15mW. The DAS uses a single input channel of a quality sound card and with input filters removed, and the data acquisition rate was 16,000 samples per second. The scattering angle θ is variable. A 90° angle was chosen as the scattering angle to record DLS time series. The distance between sample and detector can be adjusted so that the average speckle size corresponds

to the detector size (as accurately as possible) and this has been chosen as 10 cm. The transparent tube containing the aqueous suspension had a diameter of 1 cm.

The time series of scattered light intensity (TS), already recorded as described above, have been processed in several stages. First, the Fourier transform using the Fast Fourier Transform (FFT) algorithm was used to calculate the frequency spectrum of light intensity, also called power spectrum (PS). The FFT algorithm works on datasets containing a number of data points of the form $2n$, where n is a natural number, which was chosen to be 19 for TS recorded during measurements; therefore, TS had a duration of 327.680s. It was possible to achieve such a relatively large length of the TS because the suspension was stable. This produced many frequency-amplitude pairs (262,145 pairs in fact), ensuring reliable matching of the Lorentzian function.

The second step follows the original procedure of adapting the expected function for PS (power spectrum), which is the Lorentzian function, equation (27), to PS calculated on experimentally recorded TS, using a nonlinear adaptation procedure. The adjustment produces parameters a_0 and a_1 .

In (27), parameter a_0 performs vertical scaling of the spectrum, but a_1 depends on diameter d of the suspended particles, which act as scattering centers (SCs) as described by (33):

$$d = \frac{2k_B T q^2}{3\pi\eta a_1} \quad (33)$$

In (33), q is the magnitude of the scattering vector as described by equation (34):

$$q = \frac{4\pi n}{\lambda} \sin \frac{\theta}{2} \quad (34)$$

In equations (33) and (34), k_B is Boltzmann's constant, n is the refractive index of the solvent, λ is the wavelength of the laser beam, T is the absolute temperature of the solvent, η is the dynamic viscosity of the solvent, and θ is the angle used to record TS, which is usually called the scattering angle.

Recording began immediately after the liquid was transferred to the cuvette, in an automated manner, with TS lasting 34s and a delay of 29min and 26s between them. The procedure lasted 45.5h. TS was loaded into a matrix, storing 219 data in each of them, and was processed in batch mode, with average diameters as output.

The average diameter of particulate matter is calculated using equation (33). Figure 40 illustrates the calculated PS values of TS on experimental TS and adjusted Lorentzian line.

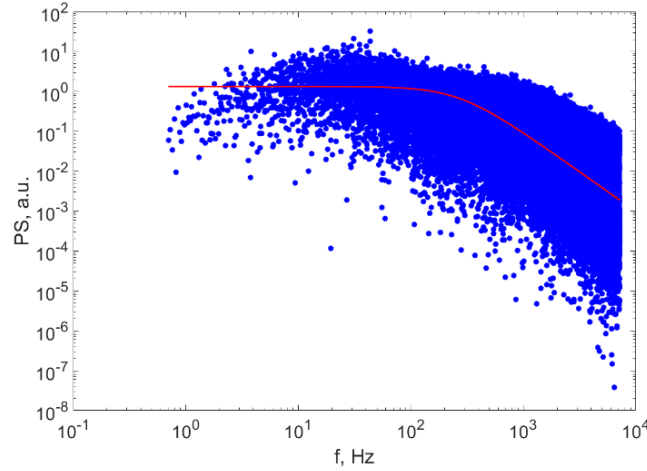


Figure 40: PS of light intensity scattered for a suspension (blue circles) and suspension-adjusted Lorentzian line (continuous line) at 10,5 h of sedimentation.

Examining the graph of the calculated PS data and the adjustment of the Lorentzian line, we note that the line sufficiently described the calculated data, which confirms the hypothesis that the distribution can be approximated as monomodal.

Error calculation

The relative error in assessing the diameter d of particles can be estimated by substituting equation (34) into equation (33) and writing the logarithm of d , as in equation (35):

$$d = \frac{32\pi k_B n^2}{3\eta a_1 \lambda^2} T \sin^2 \frac{\theta}{2} \quad (35)$$

If we consider that all constants are grouped as a single factor, the differential of that factor will be null. If we consider that the quantities we measured - and which were therefore sources of error - were the thermodynamic temperature T and the angle of measurement θ , the logarithm of d is:

$$\ln(d) = \ln \frac{32\pi k_B n^2}{3\eta a_1 \lambda^2} + \ln T + 2 \ln \left(\sin \frac{\theta}{2} \right) \quad (36)$$

If we differentiate equation (36) and consider dT and $d\theta$ to be the experimental errors in measuring these quantities, under the assumption of the worst case in which errors are summed, we obtain equation (37):

$$\varepsilon_d = \frac{\Delta d}{R} = 0 + \frac{\Delta T}{T} + \frac{1}{\tan \left(\frac{\theta}{2} \right)} \Delta \theta \quad (37)$$

The temperature measurement error was 1K for temperature T , which was 20°C, so 293.15K. The distance between detector and tube was 10 cm, and tube diameter was 1 cm, which makes $\Delta\theta$:

$$\Delta\theta = 2\alpha \tan \frac{0.5d_{tube}}{D} \quad (38)$$

Therefore, the relative error calculated using equation (37) was 10,3 %. Accordingly, the error bars of the diameters were calculated using this relative error value.

The error is relatively large but is nevertheless consistent with the purpose of the analysis, which is to use a simple configuration and data processing procedure to assess the diameter of suspended particles in aqueous suspension.

Particle size separation by sedimentation

If a particle is suspended in a fluid, it is subject to the action of three forces: gravity, float force and Stokes resistance, since the movement of very small particles occurs in laminar regime. If d is the diameter of the sprung particle, the floating force F_b , gravity G and the Stokes resistance F_s are illustrated in figure 41 and expressed as:

$$F_b = \frac{\pi}{6} d^3 \rho_0 g \quad (39)$$

$$G = \frac{\pi}{6} d^3 \rho g \quad (40)$$

$$F_s = 3\pi\eta d v \quad (41)$$

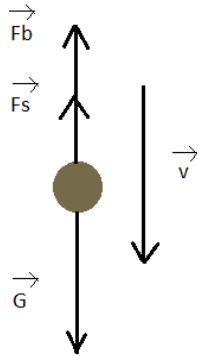


Figure 41: Forces exerted on a particle in a fluid.

In equations (39) - (41), d is the diameter of the particle, η is the dynamic viscosity of the fluid, ρ and ρ_0 are the densities of the particle and fluid, g is the gravitational acceleration, and v is the speed of the particle in the fluid. If the density of the fluid is less than the density of the particle, the velocity is directed downwards, and the particles undergo sedimentation. The fluid was deionized water with a density of 1000 kg/m^3 , and the particle density was considered to be 2648 kg/m^3 , which is the density of SiO_2 .

In equations (39) - (41), gravity and floating force are constant, but Stokes' resistance increases with velocity to the point where the vector sum of forces is zero; Therefore, the velocity remains constant and equal to a limit speed V_1 as described by equation (42):

$$v_1 = \frac{(\rho - \rho_0)d^2 g}{18\eta} \quad (42)$$

We note that the limit speed depends largely on the size of the particles, being proportional to the square of the diameter. Larger particles sediment faster than smaller ones, and this can be used to separate particles according to their size in a simple and efficient way. If we consider a vertical tube and laser beam at a distance L from the free surface of the liquid, as shown in figure 42, after a time t after pouring the fluid into the beam area, only particles that have a limit speed lower than v_m in equation (43) will remain; Therefore, they will have a smaller diameter than d_{max} described by equation (44).

$$v_m(t) = \frac{L}{t} \quad (43)$$

$$d_{max} = 3 \sqrt{\frac{3\eta v_m}{(\rho - \rho_0)}} = \sqrt{\frac{3\eta L}{(\rho - \rho_0)gt}} \quad (44)$$

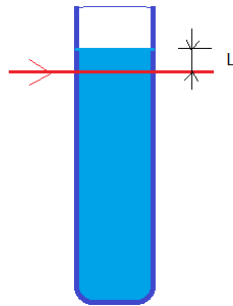


Figure 42: Sedimentation tube and laser beam.

The free surface level of the fluid has been carefully adjusted inside the sedimentation tube to position the laser beam directly below the free surface, while avoiding its reflection on the curved surface. Since water moistens the glass, the free surface is not a flat surface, but has a concave shape. With the caution described above, the distance L was estimated at 0.15 mm.

Results

Figure 43 shows a diagram of the largest diameter of particles remaining in the beam area as a function of the time elapsed since the suspension was poured, calculated using equation (44) and distance L, as mentioned above.

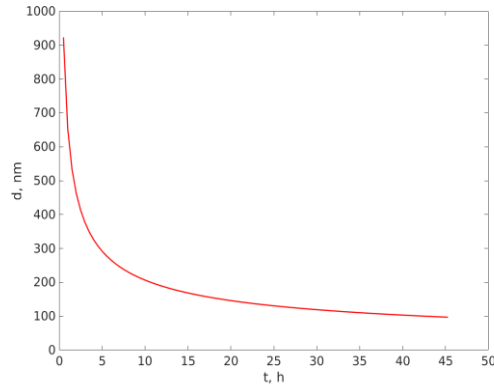


Figure 43: Maximum diameter in nm of particles still suspended in the laser beam area as a function of time t in hours.

Examining figure 43, we see that for such a small value of L, the variation in the diameter of the remaining suspended particles is quite rapid over a time interval of several tens of hours, which allows an estimate of the type and size of particles suspended in a fluid, using this very simple sedimentation experiment and the customized procedure for determining the size of DLS particles. If the particle density is greater than the fluid density, the curve shows a decrease in particle size due to sedimentation, as illustrated in figure 43. Conversely, if the particle density is less than the density of the fluid, the curve would show an increase in particle size over time as particles would move upward in the tube because the force of floatation would be greater than the force of gravity. Figure 44 illustrates the variation in the mean diameter of the remaining suspended particles in the beam area as a function of the time elapsed from the deposition of the suspension in the tube to the beginning of sedimentation.

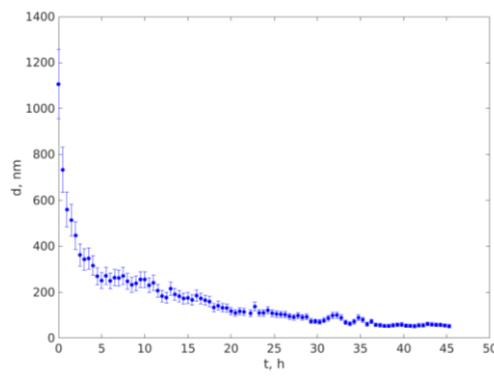


Figure 44: Variation of the mean diameter of particles remaining in the beam area during sedimentation as a function of elapsed time.

Looking at figure 44, we see that the average diameter of particles at the top of the sedimentation tube, where the beam zone was located, was about 1100 nm at the beginning of the sedimentation procedure and decreased rapidly in the first 4.5 hours to about 300 nm, followed by a slower decrease in the subsequent sedimentation hours. The apparent increases in diameter at times $t = 10\text{h}$ and $t = 32,5\text{h}$ are most likely an adjustment artifact, produced by using the same starting parameters for all time series. After 45h of sedimentation in the natural gravitational field, the largest diameter of suspended particles in the beam area was 50 nm. We should note at this point that the diameters would have continued to decrease, but the recording was stopped after 45 h. This is because it seems impractical for an experiment to take weeks, just to make the presence of particles smaller than 30 nm apparent, but most likely the distribution also contains particles smaller than 50 nm.

We also note that the best similarities of the trend in Figure 44 with the estimated diameter remaining in the beam are at $L = 0.15\text{ mm}$, calculated using equation (44) and illustrated in figure 43. If the particle density is greater than the fluid density, the curve shows a decrease in particle size due to sedimentation, as illustrated in figure 43. The very good similarity of trend and values in figures 43 and 44 is a strong indication that particulate matter harvested from rainfall had a higher density than water density. The very good similarity of the values in the two curves indicates that the particle density is very close to the density used to calculate the diameters represented in figure 43, which was 2648 kg/m^3 ; therefore, the particles deposited are most likely SiO_2 .

It should also be noted that the diameter calculated using the DLS procedure is derived from the diffusion coefficient; Therefore, this is the hydrodynamic diameter, not the physical diameter. It can realistically be understood as the diameter of diffusing particles in the form of spheres of the same diameter, regardless of their shape, which can be a rod, ellipsoid or irregular shape.

Moreover, the expected Lorentzian line match on PS calculated on experimentally recorded TS is very good, as can be seen in figure 40, which confirms that the approximation that the size distribution of particles is monomode is realistic. We must keep in mind that this approximation is consistent with the fact that the intensity of scattered light is proportional to the sixth strength of the diameter of the particles scattering at a certain angle, if the diameter is less than the wavelength, which suggests that the diameter calculated in the manner described above is not the conventionally average diameter, rather it is the average of the diameters of the largest particles suspended in the beam area.

11. Particle size measurement of automotive fluids (brake fluid and coolant) using DLS technology

A number of technological fluids, mainly used in the automotive industry, were evaluated in order to analyze the particles that are suspended in them, using the DLS technique. From the start we focused on waste fluids because the content of foreign particles in such a fluid can be an indicator for the proper functioning of an equipment or subassembly.

I have tried an engine oil analysis, but the results were not satisfactory due to the low transparency of used engine oil. In the case of oil extracted from a diesel engine, even after a run of several hundred km, it is completely black, making it impossible for the LASER beam to penetrate and scatter light by suspended particles.

Thus analysis using light scattering dynamics (DLS) technique to evaluate suspended particles was performed for brake fluid and engine coolant (antifreeze solution). The two fluids were taken from a car with an internal combustion engine, having gasoline as fuel, after a turnover of approx. 60000 km.

Fluids were taken in sterile recipient of 500 ml capacity. Since the viscosity of the two fluids was unknown, there were no data sheets of the two fluids under analysis. A mass viscosimeter was used to determine the viscosity at a temperature of 20 °C:



Figure 45: Viscosity measurements of fluids analyzed using DLS technique. On the left is the brake fluid (measured viscosity 0.0202 daP) and on the right is the coolant (measured viscosity 0.0102 daP).

Overview of DLS data processing procedure

As mentioned in the previous subchapter, the DLS technique used in this paper to characterize particles evaluates their hydrodynamic diameter.

Particles suspended in the fluid are the target of the laser beam. The coherent incident light is scattered by each particle in the beam area in all directions, producing the interference field. Since each location of the interference field contains information relating to the motion of each particle that scattered light, it is possible to evaluate information on the diffusion properties of the particles and, among them, the size of the particles. This is achieved by recording time series from a distant field location at a well-known scattering angle. For this analysis, an angle θ of 90° was used, the recorded time series are then analyzed to evaluate the diffusion coefficient; Then, from there, the size distribution of the particles or the average hydrodynamic diameter of the suspended particles.

The experimental configuration was intended to be a simple one, made with low cost common components. The configuration is shown in figure 46.

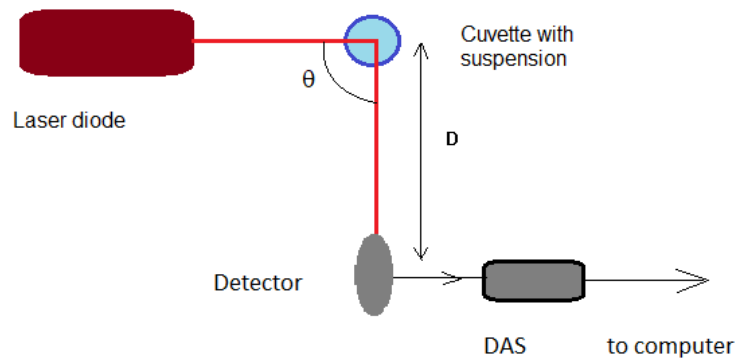


Figure 46: Experimental configuration. The dark blue circle represents the transparent bowl and the light blue disc inside represents the fluid under analysis.

The installation consists of a laser diode, a cylindrical tank containing the fluid to be analyzed, a data acquisition system (DAS), an optical detector and a computer for recording and processing time series. The wavelength of the light beam of the laser diode is 632nm. The laser diode operated in continuous mode at a power of 15mW. The optical detector was made using a PN photodiode of type SFH213 and a transimpedance preamplifier, as shown in the previous chapter. The DAS uses a channel on a sound card in which input filters have been removed. The data acquisition rate was 16,000 samples per second. The scattering angle θ , to record DLS time series, was chosen 90° . The distance between sample and detector can be adjusted so that the average speckle size corresponds as closely as possible to the size of the optical detector. The transparent tank containing the aqueous suspension is 1 cm in diameter.

The time series of scattered light intensity (TS) recorded as described above were processed in several stages. First, the Fourier transform using the Fast Fourier Transform (FFT) algorithm was used to calculate the frequency spectrum of light intensity, also called power spectrum (PS).

The second step follows the original procedure of adapting the expected function for PS (power spectrum), which is the Lorentzian function, equation (27), to PS calculated on experimentally recorded TS, using a nonlinear adaptation procedure. The adjustment produces parameters a_0 and a_1 .

In equation (27), parameter a_0 performs vertical scaling of the spectrum, but a_1 depends on the diameter d of the suspended particles, which act as scattering centers (SCs) as described by equation (33).

In equation (33), q is the magnitude of the scattering vector as described by equation (34).

In equations (33) and (34), k_B is Boltzmann's constant, n is the refractive index of the fluid, λ is the wavelength of the laser beam, T is the absolute temperature of the fluid, η is the dynamic viscosity of the fluid, and θ is the scattering angle used to record TS.

The vats containing the fluids under test were shaken for 1 minute before being placed in the test configuration. In this way we ensured that there is as homogeneous a distribution of particles as possible in the liquid mass.

The average diameter of particulate matter is calculated using equation (33). Figure 47 illustrates the calculated FS (frequency spectrum) values of TS for brake fluid measurements.

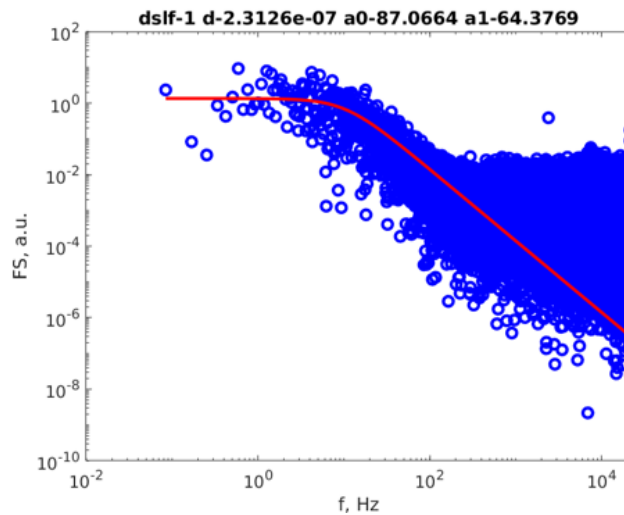


Figure 47: FS of scattered light intensity for brake fluid (blue circles) and Lorentzian line (in red).

Figure 48 illustrates the calculated FS values of TS for measurements of the coolant.

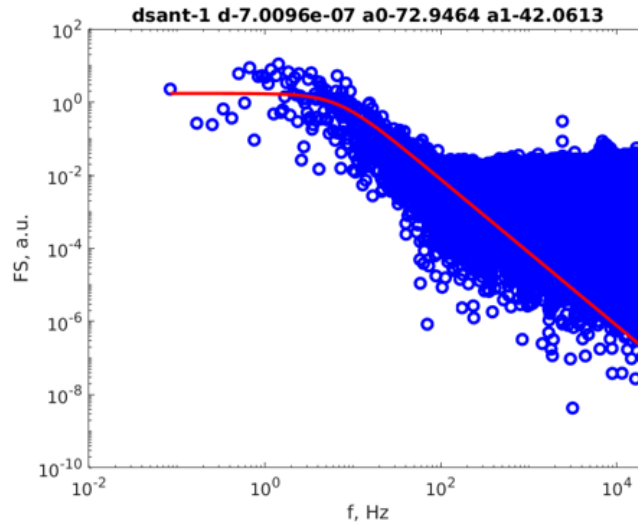


Figure 48: FS of scattered light intensity for coolant (blue circles) and Lorentzian line (in red).

Thus, parameters a_0 and a_1 were obtained and using equation (33) the average size of suspended particles in the analyzed fluids was obtained. I mention that it is about the hydrodynamic dimension.

Analyzed fluid	a_1 [Hz]	Measured viscosity [daP]	Average particle diameter [nm]	Measurement error Δt [%]
Brake fluid	64,37	0,0202	231	10,3
Coolant	42,06	0,0102	701	10,3

Figure 49: Samples analysed, parameter a_1 , measured viscosity, identified mean diameter and measurement error.

Error calculation

The relative error in assessing the diameter d of particles can be estimated, as shown in the previous chapter, by substituting equation (34) into equation (33) and writing the logarithm of d , as in equation (35).

If we consider that all constants are grouped as a single factor, the differential of that factor will be null. If we consider that the quantities we measured - and which were therefore sources of error - were the thermodynamic temperature T and the angle of measurement θ , the logarithm of d is according to the equation (36).

If we differentiate equation (36) and consider dT and $d\theta$ to be the experimental errors in measuring these quantities, under the assumption of the worst case in which the errors are summed, we obtain equation (45):

$$\varepsilon_d = \frac{\Delta d}{R} = 0 + \frac{\Delta T}{T} + \frac{1}{\tan\left(\frac{\theta}{2}\right)} \Delta\theta \quad (45)$$

The temperature measurement error was 1K for temperature T, which was 20°C, so 293.15K. The distance between detector and tube was 10cm, and tube diameter was 1cm, which makes $\Delta\theta$:

$$\Delta\theta = 2 \operatorname{atan} \frac{0.5d_{tube}}{D} \quad (46)$$

Therefore, the relative error calculated using equation (46) is 10,3 %. The error can be considered large, but nevertheless remains consistent with the purpose of analysis, which is to use a simple test configuration and data processing procedure to assess the diameter of suspended particles in process fluids.

Conclusions

Different types of fluids were analyzed using both classical laboratory methods and DLS technique.

The analysis of suspended particles in technological fluids using the stepwise filtration method is sufficient as long as we follow the characterization of large particles. The minimum size we can expect to identify should be larger than the holes of the smallest sites. Sieves are usually available with hole sizes in the range of $0.5\mu\text{m}$ – up to hundreds of μm or larger.

The procedure also requires many test steps and can take up to several hours to perform a single analysis. The necessary equipment is quite expensive and bulky.

DLS analysis, extensively exposed in this paper and used to characterize suspended particles in various technological fluids, aqueous solutions or even aerosols in air, involves almost common laboratory equipment. The sensor designed and manufactured during this study is made with high-performance components, but produced on a large scale and, consequently, at very low cost.

The described method represents a concept for the possibility of using a very simple device consisting of a tube and a laser source, even using a laser diode, for recording a temporal series of scattered light at small angles with the help of an ordinary computer sound card and processing it. For all DLS analyses presented in this paper we used as a data acquisition and processing system a personal computer with average performance and an on-board sound card, capable of acquiring signal with a sampling rate of 44,000 samples per second. The measurement itself takes a few tens of seconds for most measurements.

Depending on the specifics of the fluid in which the particles are found, there are different particularities.

For airborne particles or other gaseous media, DLS results in hydrodynamic diameter, not physical diameter. Non-spherical or irregularly shaped particles diffuse into the air. If they scatter a coherent beam of light, the waves interfere producing a DLS time series. If the time series is analysed with the procedure described, a mean hydrodynamic diameter is obtained for the purposes of DLS. Such a diameter should be understood as the diameter of equivalent spherical particles diffusing into the air, as real spherical particles do. A compact and inexpensive sensor, capable of characterizing particles in the air, can be programmed, for example, to indicate the presence of particles larger than a trigger size. Such a configuration can be used to indicate that a material burns with flame or burns muffled. It can be used as a sensor in very clean areas, such as microfabrication laboratories, in sterile medical rooms, where it can indicate the presence of viruses or bacteria, or in a technological process, where it can monitor an exhaust of flue gases to warn of the appearance of particles exceeding a certain size.

As in the case of airborne particles or other gaseous media, the diameter assessed by the DLS procedure should be regarded as the hydrodynamic diameter, which is the diameter of spherical particles diffusing as particulate matter; Therefore, the procedure does not indicate the

actual shape of the particles. In addition, the intensity of diffused light for small particles as found in suspension increases rapidly with their diameter, and the interference field is dominated by light diffused by the largest particles. The diameter assessed by the DLS procedure should be taken as the average of the largest particulate matter found in suspension at beam level; therefore, the combination of sedimentation and simple DLS procedure can be used to achieve profiling of suspended particles into liquids. It should also be considered that the fluid to be analysed has a certain degree of transparency. The lower the degree of transparency, the less light scattered and tends to zero. This could be compensated for to some extent by increasing the power of the laser emitter, but we will have hard-to-control changes in experiment parameters during measurements (such as temperature).

The goal proposed at the beginning of this road, to develop a procedure and device based on light scattering dynamics in order to assess the size of suspended particles in technological fluids, has been achieved. We obtained the characterization of particles in fluids in both liquid and gaseous states and obtained their hydrodynamic diameters using compact, simple and short-time testing equipment.

Annex - List of publications, participation in conferences and research projects

List of articles published in journals indexed in WoS:

1. An Advanced Sensor for Particles in Gases Using Dynamic Light Scattering in Air as Solvent, Chicea, D.; Leca, C.; Olaru, S.; Chicea, L.M., *Sensors* 21 (2021), no. 15, 5115. <https://doi.org/10.3390/s21155115>; revista indexată în WoS Q1
2. Profiling Particles of Sahara Dust Settled on the Ground by a Simplified Dynamic Light Scattering Procedure and Sedimentation. *International Journal of Environmental Research and Public Health*, Chicea, D.; Olaru, S.; 2023, 20(6), 4860; <https://doi.org/10.3390/ijerph2006486>, revista indexată în WoS Q1 în 09.03.2023 în momentul publicării; în 20.03.2023 revista a fost declassată și a ramas indexată în SCOPUS Q1

List of articles published in other databases:

1. Autocorrelation Function Analysis in Processing Stochastic Time Series, Silviu Rei, Dan Chicea, Sorin Olaru, *Annals of "DUNAREA DE JOS" University of Galati, Mathematics, Physics, Theoretical mechanics, Fascicle II, year VIII (XXXIX), No. 1* pp. 51-54, 2016
2. Dynamic Light Scattering Signal Conditioning for Data Processing, Silviu Mihai Rei, Dan Chicea, Beriliu Ilie, Sorin Olaru, *Acta Universitatis Cibiniensis. Technical Series* 69(1), pp.130-135, December 2017, DOI: 10.1515/aucts-2017-0016

List of papers presented orally at conferences:

1. Dynamic Light Scattering for Sizing Particles Suspended in Air – Is it Possible?, Dan CHICEA, Cristian LECA, Sorin OLARU, *International Balkan Workshop on Applied Physics Conference*, Iulie 2019, Constanta, Romania
2. Sizing Particles in Gases by an Advanced Optical Procedure, Dan Chicea, Cristian Leca and Sorin Olaru, *10 th International Conference Manufacturing Science and Education -MSE 2021-*, june 2-4, Sibiu, Romania

Conference participations with posters presented by the author:

1. Nanoparticles Size Distribution Assessment by Direct Optical Particle Tracking, Chicea D.; Maranciuc, A.; Olaru, S.; *TIM 22 Physics Conference*, 23-25 November 2022, Timisoara, Romania
2. Profiling Particles of Sahara Dust Settled in Romania by a Simplified Dynamic Light Scattering Procedure and Centrifugation, Chicea D.; Olaru, S.; *TIM 22 Physics Conference*, 23-25 November 2022, Timisoara, Romania

Participations in research projects as member of research team:

1. JINR Topical Plan: Theme code: 03-4-1128-2017/2022 Study of spatial distribution of particles in liquid media with different water content and energy parameters of ZrO₂ nanopowder dispersion system using DLS and SANS methods, Follow-up Order No. 269 item 60 and Order No. 268 item 57, Dubna și România, 2021
2. The crystalline and magnetic structure of materials developed for electrical engineering as studied by neutron scattering techniques, Follow-up, pos. 35 from the JINR Order No. nr. 269/20.05.2020

Bibliography

- 1.Lattanzio, Livio. Particulate Matter Sensing for Air Quality Measurements, Sensirion AG, Switzerland. Available online: <https://www.sensirion.com/en/about-us/newsroom/sensirion-specialist-articles/particulate-matter-sensing-for-air-quality-measurements/> (accessed on 12.06.2021)
- 2.A Cloud of Saharan Dust Reaches Romania. Available online: <https://www.romania-actualitati.ro/news-in-english/a-cloud-of-saharan-dust-reaches-romania-id147218.html> (accessed on 12` December 2022).
- 3.Berne, B.J.; Pecora, R. Dynamic Light Scattering. Courier Dover Publications (2000) ISBN 0-486-41155-9.
- 4.David Briers, Laser Doppler, Speckle and Related Techniques for Blood Perfusion Mapping and Imaging, *Physiol. Meas.* 22, R35–R66, (2001).
- 5.Huneeus, N.; Schulz, M.; Balkanski, Y.; Griesfeller, J.; Prospero, J; Kinne, S.; Bauer, S; Boucher, O.; Chin, M.; Dentener, F.; et al. Global dust model intercomparison in AeroCom phase I. *Atmos. Chem. Phys.* 2011, 11, 7781–7816.
- 6.Smoke detector. Available online: https://en.wikipedia.org/wiki/Smoke_detector (accessed on 12.06.2021)
- 7.David Briers, Donald D. Duncan, Evan Hirst, Sean J. Kirkpatrick, Marcus Larsson, WiendeltSteenbergen, Tomas Stromberg, and Oliver B. Thompson, Laser speckle contrast imaging: theoretical and practical limitations, *Journal of Biomedical Optics* 18(6), 066018(1-9), (2013).
- 8.IPCC. Climate Change 2013: The Physical Science Basis; IPCC: Geneva, Switzerland, 2013.
- 9.Tang, Dong; Ju, Zhixuan; Wang, Li. Simulation and Experimental Research on the Charged Characteristics of Particulate Matter in the Sensor under Different Exhaust States. *Sensors* 2020, 20(21), 6226.
- 10.Balkanski, Y.; Schulz, M.; Claquin, T.; Guibert, S. Reevaluation of Mineral aerosol radiative forcings suggests a better agreement with satellite and Aeronet data, *Atmos. Chem. Phys.* 2007, 7, 81–95. <https://doi.org/10.5194/acp-7-81-2007>.
- 11.Chicea D., Biospeckle Size and Contrast Measurement Application in Particle Sizing and Concentration Assessment, *Romanian Journal of Physics*, Vol. 52, Numbers 5-7, pp. 581-587, (2007).
- 12.Duric, Aleksandar. Principles of ASA fire-detection technology. Published by Siemens Switzerland Ltd. Available online: <https://www.downloads.siemens.com/download-center/Download.aspx?pos=download&fct=getasset&id1=A6V10646105> (accessed on 13.06.2021)
- 13.Air Photon Integrating Nephelometers. AirPhoton. Available online: https://www.airphoton.com/uploads/7/6/0/6/76064899/airphoton_nephelometers.pdf (accessed on 13.06.2021)
- 14.Chicea D., Coherent Light Scattering on Nanofluids - Computer Simulation Results, *Applied Optics*, Vol. 47, No. 10, pp. 1434-1442, (2008).
- 15.Milford, C.; Cuevas, E.; Marrero, C.L.; Bustos, J.; Gallo, V.; RodrÁguez, S.; Romero-Campos, P.M.; Torres, C. Impacts of Desert Dust Outbreaks on Air Quality in Urban Areas. *Atmosphere* 2020, 11, 23.
- 16.Chicea D., Application of Whole Blood Coherent Light Scattering Dynamics Analysis *Journal of Optoelectronics and Advanced Materials*, Vol. 10, No. 8, pp. 2163-2167, (2008).
- 17.INTEGRATING NEPHELOMETER 3563. TSI Incorporated. Available online: https://www.arm.gov/publications/tech_reports/handbooks/nephelometer_handbook.pdf (accessed on 13.06.2021)
- 18.Neophytou, A.M.; Yiallourous, P.; Coull, B.A.; Kleanthous, S.; Pavlou, P.; Pashiardis, S.; Dockery, D.W.; Koutrakis, P.; Laden, F. Particulate matter concentrations during desert dust outbreaks and daily mortality in Nicosia, Cyprus. *J. Expo. Sci. Environ. Epidemiol.* 2013, 23, 275–280.
- 19.Chicea D., Revealing FE3O4 Nanoparticles Aggregation Dynamics Using Dynamic Light Scattering, *Optoelectronics and Advanced Materials – Rapid Communications* vol. 3, no. 12, pp. 1299 – 1305, (2009).

20. Mallone, S.; Stafoggia, M.; Faustini, A.; Gobbi, G.P.; Marconi, A.; Forastiere, F. Saharan Dust and Associations between Particulate Matter and Daily Mortality in Rome, Italy. *Environ. Health Perspect.* 2011, 119, 1409–1414.
21. Mariani Idroas; Ruzairi Abdul Rahim; Robert Garnet Green; Muhammad Nasir Ibrahim; Mohd Hafiz Fazalul Rahiman. Image Reconstruction of a Charge Coupled Device Based Optical Tomographic Instrumentation System for Particle Sizing. *Sensors* 2010, 10, 9512-9528.
22. Chicea D., Chicea R., Chicea L. M., Using Chordin to Simulate Coherent Light Scattering Dynamics on Biological Suspensions, *Romanian Journal of Biophysics*, Vol. 20, No. 2, pp. 157–170, (2010).
23. Ejay Nsugbe; Cristobal Ruiz-Carcel; Andrew Starr; Ian Jennions. Estimation of Fine and Oversize Particle Ratio in a Heterogeneous Compound with Acoustic Emissions. *Sensors* 2018, 18(3), 851.
24. Sand, W.; Advisory, D.S.W. WMO Airborne Dust Bulletin; WMO: Geneva, Switzerland, 2018.
25. Carlson, T.N.; Prospero, J.M. The Large-Scale Movement of Saharan Air Outbreaks over the Northern Equatorial Atlantic. *J. Appl. Meteorol. Climatol.* 1972, 11, 283–297.
26. Clark N.A.; Lunacek J.H.; Benedek G.B. A study of Brownian motion using light scattering. *American Journal of Physics* 1970, 38(5), 575-585.
27. Ben-Ami, Y.; Koren, I.; Rudich, Y.; Artaxo, P.; Martin, S.T.; Andreae, M.O. Transport of North African dust from the Bodélé depression to the Amazon Basin: A case study. *Atmos. Chem. Phys.* 2010, 10, 7533–7544.
28. Chicea D., A Study of Nanoparticle Aggregation by Coherent Light Scattering, *Current Nanoscience*, vol. 8 issue 6, pp. 259-265, 2012, doi: <http://dx.doi.org/10.2174/157341312800167704>.
29. Barkan, J.; Kutiel, H.; Alpert, P.; Kishcha, P. Synoptics of dust intrusion days from the African continent into the Atlantic Ocean. *J. Geophys. Res. Atmos.* 2004, 109. <https://doi.org/10.1029/2003jd004416>.
30. Chicea D., Indrea E., Cretu C. M., Assessing FE₃O₄ Nanoparticle Size by DLS, XRD AND AFM, *Journal of Optoelectronics and Advanced Materials* Vol: 14, Issue: 5-6, pp: 460-466, (2012).
31. Chicea D., Revealing FE₃O₄ Nanoparticle Aggregation in Aqueous Suspension by Nonconventional Optical Methods, *Journal of Optoelectronics And Advanced Materials* Vol. 15, No. 9 - 10, pp. 982 – 988, (2013).
32. Tchordadjieff, A.; Angelov, C.; Arsov, T.; Nikolova, N.; Kalapov, I.; Boyadjieva, A. Sahara dust events over south-western Bulgaria during the late spring of 2013. *Comptes Rend. l'Acad. Bulg. Sci.* 2015, 68, 1229.
33. Chicea D., A Simple Algorithm to Simulate Nanoparticles Motion in a Nanofluid, *U.P.B. Sci. Bull., Series A*, Vol. 76, Iss. 2, pp: 199-206, (2014).
34. Khintchine, Alexander. Korrelationstheorie der stationären stochastischen Prozesse. *Mathematische Annalen* 1934, 109 (1), 604–615. doi:10.1007/BF01449156.
35. Reiff, J.; Forbes, G.S.; Spiexsma, F.T.M.; Reynders, J.J. African Dust Reaching Northwestern Europe: A Case Study to Verify Trajectory Calculations. *J. Clim. Appl. Meteorol.* 1986, 25, 1543–1567.
36. B. Chu, *Laser Light Scattering: Basic Principles and Practice* (Academic, Boston, 1991).
37. Hamonou, E.; Chazette, P.; Balis, D.; Dulac, F.; Schneider, X.; Galani, E.; Ancellet, G.; Papayannis, A. Characterization of the vertical structure of Saharan dust export to the Mediterranean basin. *J. Geophys. Res. Atmos.* 1999, 104, 22257–22270.
38. M. Kaszuba et al., Protein and Nanoparticle Characterisation Using Light Scattering Techniques, *Part. Part. Syst. Charact.*, 2006, 23, 193-196.
39. Papayannis, A.; Amiridis, V.; Mona, L.; Tsaknakis, G.; Balis, D.; Bosenberg, J.; Begue, N.; Tulet, P.; Pelon, J.; Aouizerats, B.; et al. Aerosol processing and CCN formation of an intense Saharan dust plume during the EUCAARI 2008 campaign. *Atmos. Chem. Phys.* 2015, 15, 3497–3516.
40. Ansmann, A.; Bösenberg, J.; Chaikovskiy, A.; Comerón, A.; Eckhardt, S.; Eixmann, R.; Freudenthaler, V.; Ginoux, P.; Komguem, L.; Linné, H.; et al. Long-range transport of Saharan dust to northern Europe: The 11–16 October 2001 outbreak observed with EARLINET. *J. Geophys. Res. Atmos.* 2003, 108. <https://doi.org/10.1029/2003JD003757>.
41. P. Stepanek, “Data analysis in dynamic light scattering,” *Dynamic Light Scattering*, W. Brown, ed. (Oxford University, Oxford, UK, 1993), pp. 177–240.

42. Provencher, S. CONTIN: A general purpose constrained regularization program for inverting noisy linear algebraic and integral equations. *Computer Physics Communications* 1982, 27 (3), 229-242, doi:10.1016/0010-4655(82)90174-6.
43. Chicea D., Rei S., Leca C. Monitoring yeast cells size during fermentation using dynamic light scattering, 9th Central European Congress on Food 26.05.2018
44. Franzen, L.G.; Hjelmroos, M.; Kallberg, P.; Brorstrom-Lunden, E.; Juntto, S.; Savolainen, A.L. The 'yellow snow episode' of northern Fennoscandia, March 1991—A case study of long-distance transport of soil, pollen and stable organic compounds. *Atmos. Environ.* 1994, 28, 3587–3604.
45. Provencher, S. W. A constrained regularization method for inverting data represented by linear algebraic or integral equations. *Computer Physics Communications* 1982, 27 (3), 213–227, doi:10.1016/0010-4655(82)90173-4.
46. Bencherif, H.; Bounhir, A.; Bègue, N.; Millet, T.; Benkhaldoun, Z.; Lamy, K.; Portafaix, T.; Gadouali, F. Aerosol Distributions and Sahara Dust Transport in Southern Morocco, from Ground-Based and Satellite Observations. *Remote Sens.* 2022, 14, 2454. <https://doi.org/10.3390/rs14102454>.
47. Haywood, J.; Francis, P.; Dubovik, O.; Glew, M.; Holben, B. Comparison of aerosol size distributions, radiative properties, and optical depths determined by aircraft observations and Sun photometers during SAFARI 2000. *J. Geophys. Res. Atmos.* 2003, 108, 8471. <https://doi.org/10.1029/2002JD002250>.
48. Craig I. J. D.; Thompson A. M.; and Thompson W. J. Practical Numerical Algorithms Why Laplace Transforms Are Difficult To Invert Numerically. *Computers in Physics* 1994, 8, 648, doi: 10.1063/1.4823347.
49. Piederrière, Y.; Le Meur, J.; Cariou, J.; Abgrall, J.F.; Blouch, M.T. Particle aggregation monitoring by speckle size measurement; application to blood platelets aggregation. *Opt. Express* 2004, 12, 4596–4601.
50. Venzac, H.; Sellegri, K.; Villani, P.; Picard, D.; Laj, P. Seasonal variation of aerosol size distributions in the free troposphere and residual layer at the puy de Dôme station, France. *Atmos. Chem. Phys.* 2009, 9, 1465–1478. <https://doi.org/10.5194/acp-9-1465-2009>.
51. Chauvigné, A.; Sellegri, K.; Hervo, M.; Montoux, N.; Freville, P.; Goloub, P. Comparison of the aerosol optical properties and size distribution retrieved by sun photometer with in situ measurements at midlatitude. *Atmos. Meas. Tech.* 2009, 9, 4569–4585. <https://doi.org/10.5194/amt-9-4569-2016>.
52. Piederrière, Y.; Cariou, J.; Guern, Y.; Le Jeune, B.; Le Brun, G.; Lotrian, J. Scattering through fluids: Speckle size measurement and Monte Carlo simulations close to and into the multiple scattering. *Opt. Express* 2004, 12, 176–188.
53. Mahowald, N.; Albani, S.; Kok, J.F.; Engelstaeder, S.; Scanza, R.; Ward, D.S.; Flanner, M.G. The size distribution of desert dust aerosols and its impact on the Earth system. *Aeolian Res.* 2014, 15, 53–71. <https://doi.org/10.1016/j.aeolia.2013.09.002>.
54. Tscharnuter W. *Encyclopedia of Analytical Chemistry*; John Wiley & Sons: Hoboken-New Jersey, USA, 2006.
55. Goodman, J.W. Statistical properties of laser speckle patterns. In *Laser Speckle and Related Phenomena*; Springer: Berlin/Heidelberg, Germany, 1984; pp. 9–75.
56. Hinds, W.C. *Aerosol Technology: Properties, Behavior, and Measurement of Airborne Particles*, 2nd ed.; John Wiley & Sons: New York, NY, USA, 1999.
57. ST operational amplifiers, application notes, <https://www.st.com/en/amplifiers-and-comparators/operational-amplifiers-op-amps.html>
58. Weiner B.B. *Liquid and Surface Borne Particle Measurement Handbook*; Taylor & Francis: New York, USA, 1996.
59. Berne B.J.; Pecora R. *Dynamic Light Scattering: With Applications to Chemistry, Biology, and Physics*; Dover Publications: Mineola, U.S.A., 2000; pp. 164-206.
60. Gillette, D.A.; Blifford, I.H.; Fenster, C.R. Measurements of aerosol size distributions and vertical fluxes of aerosols on land subject to wind erosion. *J. Appl. Meteorol.* 1972, 11, 977–987.
61. Kataoka, T.; Inoue, H.; Endo, K.; Oshikane, Y.; Mori, Y.; Nakano, M.; Wada, K.; An, H. Light scattering by small particles and small defects on the silicon wafer surface. Calculations of scattering light intensity and optical image through a lens. *J. Jpn. Soc. Precis. Eng.* 2000, 66, 1716–1722.

- 62.Reid, E.A.; Reid, J.S.; Meier, M.M.; Dunlap, M.R.; Cliff, S.S.; Broumas, A.; Perry, K.; Maring, H. Characterization of African dust transported to Puerto Rico by individual particle and size segregated bulk analysis. *J. Geophys. Res. Atmos.* 2003, 108, 8591. <https://doi.org/10.1029/2002JD002935>.
- 63.Wiener, Norbert. Generalized Harmonic Analysis. *Acta Mathematica* 1930, 55, 117–258. doi:10.1007/bf02546511
- 64.Xu, R. Particle characterization: Light scattering methods. *China Particuol.* 2003, 1, 271.
- 65.Stetefeld, J.; McKenna, S.A.; Patel, T.R. Dynamic light scattering: A practical guide and applications in biomedical sciences. *Biophys. Rev.* 2016, 8, 409–427.
- 66.Wishard, A.; Gibb, B.C. Dynamic Light Scattering—An all-purpose guide for the supramolecular chemist. *Supramol. Chem.* 2019, 31, 608–615. <https://doi.org/10.1080/10610278.2019.1629438>.
- 67.Berdnik, V.V.; Loiko, V.A. Retrieval of size and refractive index of spherical particles by multiangle light scattering: Neural network method application. *Appl. Opt.* 2009, 48, 6178–6187.
- 68.Chicea, Dan; Leca, Cristian. Investigation on the Possibility of Designing an Educational Dynamic Light Scattering Device for Sizing Particles Suspended in Air. *Balkan Region Conference on Engineering and Business Education, Sibiu, Romania, 2020; vol.3, no.1, pp.154-161.* <https://doi.org/10.2478/cplbu-2020-0018>
- 69.Pecora, R. Doppler Shifts in Light Scattering from Pure Liquids and Polymer Solutions. *J. Chem. Phys.* 1964, 40, 1604–1614.
- 70.Berdnik, V.V.; Mukhamedjarov, R.D.; Loiko, V.A. Characterization of optically soft spheroidal particles by multiangle light-scattering data by use of the neural-networks method. *Opt. Lett.* 2004, 29, 1019–1021.
- 71.Cummins, H.Z.; Knable, N.; Yeh, Y. Observation of Diffusion Broadening of Rayleigh Scattered Light. *Phys. Rev. Lett.* 1964, 12, 150–153.
- 72.Sutherland W. The viscosity of gases and molecular force. *The London, Edinburgh, and Dublin Philosophical Magazine and Journal of Science* 1893, 36, 507-31.
- 73.Chicea, D., Using neural networks for dynamic light scattering time series processing. *Measurement Science and Technology* 2017, 28, 055206
- 74.Dubin, S.B.; Lunacek, J.H.; Benedek, G.B. Observation of the spectrum of light scattered by solutions of biological macromolecules. *Proc. Natl. Acad. Sci. USA* 1967, 57, 1164–1171. <https://doi.org/10.1073/pnas.57.5.1164>.
- 75.McGovern, P.E. *Ancient Wine: The Scientific Search for the Origins of Viniculture*; Princeton University Press: Princeton, NJ, USA, 2003.
- 76.Cavaliere, D.; McGovern, P.E.; Hartl, D.L.; Mortimer, R.; Polsinelli, M. Evidence for *S. cerevisiae* fermentation in ancient wine. *J. Mol. Evol.* 2003, 57, S226–S232.
- 77.Chicea, D.; Rei S.M. A fast artificial neural network approach for dynamic light scattering time series processing. *Measurement Science and Technology* 2018, 29, 105201
- 78.Engineering ToolBox. Particle Sizes 2005. [online] Available at: https://www.engineeringtoolbox.com/particle-sizes-d_934.html (Accessed 16.06.2021).
- 79.Goodman, J.W. *Statistical Optics*; Wiley Classics Library Edition; John Wiley & Sons, Inc.: Hoboken, NJ, USA, 2000.
- 80.McGovern, P.E.; Hartung, U.; Badler, V.R.; Glusker, D.L.; Exner, L.J. The beginnings of winemaking and viniculture in the ancient Near East and Egypt. *Expedition* 1997, 39, 3–21.
- 81.Carrieri, A.H. Neural network pattern recognition by means of differential absorption Mueller matrix spectroscopy. *Appl. Opt.* 1999, 38, 3759–3766.
- 82.Chicea, D; Neamtu, B; Chicea, R; Chicea, L. M. THE APPLICATION OF AFM FOR BIOLOGICAL SAMPLES IMAGING. *DIGEST JOURNAL OF NANOMATERIALS AND BIOSTRUCTURES* Volume: 5, Issue: 4, pages: 1015-1022
- 83.Hecht, E. *Optics*; Addison-Wesley: New York, NY, USA, 2001.
- 84.Chicea, D. USING AFM TOPOGRAPHY MEASUREMENTS IN NANOPARTICLE SIZING. *Romanian Reports in Physics* 2014, Vol. 66, No. 3, P. 778–787,

- 85.Chicea, D; Chicea, R.; Chicea, L.M. HSA PARTICLE SIZE CHARACTERIZATION BY AFM. Romanian Reports in Physics 2013, Vol. 65, No. 1, P. 178–185,
- 86.Koppel, D.E. Analysis of Macromolecular Polydispersity in Intensity Correlation Spectroscopy: The Method of Cumulants. J. Chem. Phys. 1972, 57, 4814–4820.
- 87.Morrison, I.D.; Grabowski, E.F.; Herb, C.A. Improved techniques for particle size determination by quasi-elastic light scattering. Langmuir 1985, 1, 496–501.
- 88.Ulanowski, Z.; Wang, Z.; Kaye, P.H.; Ludlow, I.K. Application of neural networks to the inverse light scattering problem for spheres. Appl. Opt. 1998, 37, 4027–4033.
- 89.Shabanov, A.E.; Petrov, M.N.; Chikitkin, A.V. A multilayer neural network for determination of particle size distribution in dynamic light scattering problem. Comput. Res. Model. 2019, 11, 265–273.
- 90.Beale, H.D.; Demuth, H.B.; Hagan, M.T.; DeJesus, O. Neural Network Design. Available online: <https://hagan.okstate.edu/NNDesign.pdf> (accessed on 5 August 2019).
- 91.Langowski, J.; Bryan, R. Maximum entropy analysis of photon correlation spectroscopy data using a Bayesian estimate for the regularization parameter. Macromolecules 1991, 24, 6346–6348. <https://doi.org/10.1021/ma00023a045>.
- 92.Levenberg, K. A method for the solution of certain non-linear problems in least squares. Q. Appl. Math. 1944, 2, 164–168.
- 93.Jaynes, E.T. Information Theory and Statistical Mechanics. Phys. Rev. 1957, 106, 620–630. <https://doi.org/10.1103/PhysRev.106.620>.
- 94.TI OPA320 Datasheets and application notes, <https://www.ti.com/product/OPA320>
- 95.Davies, B.; Martin, B. Numerical Inversion of the Laplace Transform: A Survey and Comparison of Methods. J. Comput. Phys. 1979, 33, 1–32.
- 96.TI TINA simulation tool, <https://www.ti.com/tool/TINA-TI?keyMatch=TINA>
- 97.OSRAM SFH datasheets and application notes, <https://ams-sram.com/products/photodetectors/photodiodes/osram-radial-t1-34-sfh-213>
- 98.Gurney, K. An Introduction to Neural Networks; Taylor & Francis e-Library: London, UK, 2004.
- 99.KIKAD design tool, <https://www.kicad.org/>
- 100.Haykin, S. Neural Networks and Learning Machines Third Edition—University Hamilton; Prentice Hall: Hoboken, NJ, USA, 2008.
- 101.Fiore, J. M. Operational Amplifiers & Linear Integrated Circuits: Theory and Application / 3E, Version 3.2.6, 07 May 2021, ISBN13: 978-1796856897
- 102.Chicea, D. An Artificial Neural Network Assisted Dynamic Light Scattering Procedure for Assessing Living Cells Size in Suspension. Sensors 2020, 20, 3425. <https://doi.org/10.3390/s20123425>.
- 103.Chicea, D.; Leca, C.; Olaru, S.; Chicea, L.M. An Advanced Sensor for Particles in Gases Using Dynamic Light Scattering in Air as Solvent. Sensors 2021, 21, 5115. <https://doi.org/10.3390/s21155115>.
- 104.Saqib, F.; Aslam, M.A.; Mujahid, K.; Marceanu, L.; Moga, M.; Ahmedah, H.T.; Chicea, L. Studies to Elucidate the Mechanism of Cardio Protective and Hypotensive Activities of *Anogeissus acuminata* (Roxb. ex DC.) in Rodents. Molecules 2020, 25, 3471. <https://doi.org/10.3390/molecules25153471>.
- 105.Cooley, J.W.; Tukey, J.W. An Algorithm for the Machine Computation of the Complex Fourier Series. Math. Comput. 1965, 19, 297–301.
- 106.Duhamel, P.; Vetterli, M. Fast Fourier Transforms: A Tutorial Review and a State of the Art. Signal Process. 1990, 19, 259–299.
- 107.Chicea, D.; Chicea, L.M. Results of light scattering dynamics analysis of biological fluids. J. Optoelectron. Adv. Mater. 2007, 9, 694–697.
- 108.Chicea, D.; Chicea, R.; Chicea, L.M.; Bunoiu, M.; Malaescu, I. Using DLS for Fast Urine Sample Analysis. AIP Conf. Proc. 2010, 1262, 150–154.